Chinese Journal of Chemical Engineering 90 (2026) 308–325

Contents lists available at ScienceDirect

Chinese Journal of Chemical Engineering

journal homepage: www.elsevier.com/locate/CJChE

Full Length Article

Comparative evaluation of interphase mass transfer models for co- and counter-current bubble columns using two-fluid CFD-PBM simulations

Keran Li [1], Xi Ma [1], Shuai Yan [2], Caixia Chen [1], Zihong Xia [1,*]

[1] Department of Energy and Chemical Engineering, East China University of Science and Technology, Shanghai 200237, China
[2] School of Materials and Chemical Engineering, Ningbo University of Technology, Ningbo 315211, China

ARTICLE INFO

Article history:
Received 23 July 2025
Received in revised form
28 September 2025
Accepted 29 September 2025
Available online 30 October 2025

Keywords:
Interphase mass transfer model
CFD-PBM simulation
Co- and counter-current flows
Bubble column

ABSTRACT

Interphase mass transfer in gas–liquid bubble columns is commonly modeled using three distinct theoretical frameworks: single-bubble theory, gas–liquid slip velocity assumption, and eddy-bubble interactions. This study presents, for the first time, a comparative computational fluid dynamic–population balance model (CFD-PBM) evaluation under both co-current and counter-current flows, systematically assessing five established models—Ranz–Marshall and Brauer (single-bubble model), Higbie and Bird (slip velocity model), and Kawase (eddy cell model)—within the ANSYS Fluent two-fluid framework. The simulations are rigorously validated against experimental CO_2 absorption/desorption data encompassing both co-current and counter-current flow configurations. Results indicate that the Kawase eddy cell model shows agreement within ±15% with experimental measurements, particularly under counter-current conditions, due to its incorporation of turbulence effects. While the single-bubble model (Brauer) and the slip velocity approach (Higbie and Bird) reproduce qualitative trends, they exhibit considerable quantitative deviations. The Ranz–Marshall model proves inadequate for accurate mass transfer predictions. Analysis of bubble size distribution reveals its strong dependence on flow regimes. Notably, counter-current operation significantly enhances mass transfer performance compared to co-current flow, primarily through increased gas holdup and enhanced turbulent mixing. These insights offer valuable guidance for both model selection and the design optimization of bubble column reactors.

1. Introduction

Bubble columns are widely used in chemical, biochemical, and environmental engineering due to their simple structure and excellent mass transfer performance. Depending on the flow directions of gas and liquid, bubble columns can operate in batch, co-current, or counter-current flow modes. In batch or semi-batch operations, and in co-current flow configurations, bubble columns are predominantly employed in the chemical and metallurgical industries. In contrast, counter-current bubble columns are commonly applied in processes such as gas absorption, desulfurization, and biochemical water treatment. The interfacial mass transfer in these systems is significantly influenced by the hydrodynamics, which vary depending on the operational mode.

In past years, experimental studies have primarily focused on hydrodynamic characteristics of bubble columns, including gas holdup, regime transition, and turbulence properties under different operation modes. First, regarding the gas holdup characteristics, co-current flow generally accelerates bubble rise and reduces gas holdup, whereas counter-current liquid flow tends to retard bubble rise and increase gas holdup [1,2]. It should be noted that bubble acceleration effects become negligible in both flow configurations when liquid velocities are significantly lower than bubble rise velocities [2,3]. Second, concerning flow regime transition, significant differences exist between counter-current and co-current flows. Specifically, a pseudo-non-uniform flow state emerges in counter-current flows with increasing liquid phase flow rates [4]. Third, with respect to turbulence characteristics, operational modes exhibit distinct influences. In batch mode, increasing gas flow rate enhances liquid recirculation, resulting in elevated shear rates in the vertical direction. In contrast, counter-current flow mainly shifts the liquid velocity profile downward without substantially

* Corresponding author.
E-mail address: zihxia@ecust.edu.cn (Z. Xia).

https://doi.org/10.1016/j.cjche.2025.09.021

altering the time-averaged shear rate [5]. Furthermore, counter-current bubble columns demonstrate significantly enhanced turbulence at high gas holdup conditions. This phenomenon can be attributed to the increased gas–liquid interfacial area associated with higher gas holdup, which consequently improves mass transfer efficiency [5,6].

Turbulence in the gas–liquid flow plays a crucial role in interfacial mass transfer within bubble columns. Han *et al.* [7] suggested that turbulence in the dissipative region contributed to a large fraction of the total mass transfer rate and that the effect of turbulence in the inertial subrange cannot be neglected. Fortescue and Pearson [8] argued that large-scale eddies dominated the convective effect of turbulence on mass transfer. However, the effect of different operation modes on the mass transfer is not yet well understood.

To clarify these complex hydrodynamics and mass transfer interactions, numerical methods like CFD are increasingly applied [9–13]. For instance, Rzehak and Krepper [9] performed two-dimensional simulations of CO_2 physical absorption in a co-current bubble column and demonstrated that the ideal gas law significantly influences simulation results, particularly in slender columns. Similarly, Khan *et al.* [12] numerically simulated mass transfer in counter-current flow and successfully predicted bubble shrinkage due to CO_2 absorption. However, these studies adopted a fixed mass transfer coefficient across different operation modes, which relies heavily on empirical correlations or experimental data. Consequently, the mass transfer process was not fully coupled with the underlying complex hydrodynamics.

A reliable mass transfer model is crucial for accurately describing transport phenomena in gas–liquid flow systems. Four predominant model types have been developed: (a) single bubble-based models [14,15], (b) slip velocity models [16,17], (c) surface renewal/stretch models [18], and (d) eddy cell models [19,20]. Single bubble-based models (*e.g.*, Ranz—Marshall [14] and Brauer [15]) incorporate both molecular diffusion and convective mass transfer through empirical or semi-empirical formulations. However, their model coefficients, typically derived from extensive experimental data, inherently limit their applicability range. The slip velocity model [16,17], rooted in Higbie's penetration theory and solved using Fick's second law, advanced the understanding of interphase mass transfer by characterizing the process through non-stationary diffusion. This formulation offered improved predictive capability for gas–liquid flows relative to preceding models. Building upon this foundation, the surface renewal model [18] further refined the approach by incorporating the stochastic nature of contact time between liquid microelements and interfaces. Both models exhibit strong agreement with experimental data in low-flow regimes [21–24]. Eddy cell models provide a more comprehensive approach by solving the convection-diffusion equation for turbulent eddies across all relevant scales, including the Kolmogorov micro-scale [7,19,20]. These models fundamentally assume that mass transfer is primarily controlled by small-scale eddies, establishing a direct coupling between turbulent energy dissipation and mass transfer rates. This framework enables more accurate predictions in complex flow regimes where traditional models fail. Lamont's foundational eddy cell model [19] specifically addressed the role of dissipation-range eddies, while Han *et al.* [7] made subsequent progress through their eddy contact model by incorporating energy spectrum analysis to characterize multiscale eddy contributions. The predicted mass transfer coefficient showed a better agreement with experimental data, and confirmed that eddies in the dissipation range contribute to the major part of the overall mass-transfer rate.

Different mass transfer models have been used in computational fluid dynamics–population balance model (CFD-PBM) simulations of the interphase mass transfer in gas–liquid flows. In a semi-batch bubble column, Zhang *et al.* [25] used the slip velocity model and eddy cell model, and found that the mass transfer rates decreased with the liquid viscosity increasing. Wang *et al.* [26] compared simulation results using eddy cell model and surface renewal model and found that an eddy cell model developed by Lamont and Scott [19] performed reasonably. Guo *et al.* [27] coupled the Higbie model with CFD-PBM to investigate the impact of different liquid phase properties on gas–liquid mass transfer and bubble coalescence and break-up. In co-current bubble columns, Li *et al.* [28] investigated the applicability of different mass transfer models with focus on the effects of bubble-induced turbulence on mass transfer. However, previous studies often rely on fixed bubble diameter or fixed mass transfer coefficients, lacking comparisons of different model types (single-bubble, slip velocity, eddy-cell) under varying flow regimes.

This paper presents simultaneous evaluations of physical absorption and desorption of carbon dioxide in both co- and counter-current modes using validated 3D simulations. Three types of mass transfer models were systematically examined with the experimental data by Deckwer *et al.* [29]. The limitations of these models were analyzed and the differences of mass transfer characteristics observed in co-current and counter-current bubble columns were discussed.

2. Simulation Model

2.1. Governing equations for two-fluid model

The Eulerian two-fluid model is used for the simulations of gas–liquid bubble columns. In the model, both the liquid and the gas phases are treated as continuous fluid. The continuity and the momentum conservation equations of phase q are written as:

$$\frac{\partial(\alpha_q\rho_q)}{\partial t}+\nabla\cdot(\alpha_q\rho_q\boldsymbol{u}_q)=\dot{m}_q \tag{1}$$

$$\begin{aligned}\frac{\partial(\alpha_q\rho_q\boldsymbol{u}_q)}{\partial t}+\nabla\cdot(\alpha_q\rho_q\boldsymbol{u}_q\boldsymbol{u}_q)=&-\alpha_q\nabla p+\alpha_q\rho_q\boldsymbol{g}\\&+\nabla\cdot\left[\alpha_q\mu_{\mathrm{eff},q}\left(\nabla\boldsymbol{u}_q+\nabla\boldsymbol{u}_q{}^{\mathrm{T}}\right)\right]+\boldsymbol{M}_q\end{aligned} \tag{2}$$

where α_q, $\mu_{\mathrm{eff},q}$ are the volume fraction and the effective viscosity of the phase q, respectively. The subscript q represents gas phase (G) or liquid phase (L).

In the continuity equation of gas phase, the gas density is determined using the ideal-gas law to consider the effect of hydrostatic pressure [9,10,12,28]. $\dot{m}_q$ represents the mass source of interfacial mass transfer between the gas and liquid phase. In Eq. (2), $\boldsymbol{M}_q$ represents the interphase forces between the two phases. In the simulations, the forces due to the interfacial drag, the lift effects, turbulent dispersion and the wall lubrications are considered and the models are listed in Table 1. This model

Table 1
Summary of the interfacial force models.

Force	Model
Drag	Tomiyama [30]
Lift	Tomiyama *et al.* [31]
Turbulent dispersion	Burns *et al.* [32]
Wall lubrication	Hosokawa *et al.* [33]

combination has been validated in prior CFD studies of the Deckwer experiment (*e.g.*, Rzehak and Krepper [9], Li *et al.* [28]), with results consistent with experimental measurements, thereby supporting the current model selection.

2.2. Turbulence model

The dispersed RNG k–ε model has been validated in previous studies for its accuracy in simulating turbulence in gas–liquid flows [34,35]. The governing equations for turbulent kinetic energy k and dissipation rate ε of the liquid phase are expressed as:

$$\frac{\partial(\alpha_L\rho_L k)}{\partial t}+\nabla\cdot(\alpha_L\rho_L\boldsymbol{u}_L k)=\nabla\cdot\left[\alpha_L\left(\mu_{m,L}+\rho_L C_\mu\frac{k^2}{\varepsilon\sigma_k}\right)\nabla k\right]+\alpha_L\left(G_{k,L}-\alpha_L\rho_L\boldsymbol{\varepsilon}\right)+\alpha_L\rho_L\Pi_{k,L} \tag{3}$$

$$\frac{\partial(\alpha_L\rho_L\varepsilon)}{\partial t}+\nabla\cdot(\alpha_L\rho_L\boldsymbol{u}_L\varepsilon)=\nabla\cdot\left[\alpha_L\left(\mu_{m,L}+\rho_L C_\mu\frac{k^2}{\varepsilon\sigma_\varepsilon}\right)\nabla\varepsilon\right]+\frac{\alpha_L\boldsymbol{\varepsilon}}{k}\left(C_{1\boldsymbol{\varepsilon}}G_{k,L}-C_{2\boldsymbol{\varepsilon}}\rho_L\boldsymbol{\varepsilon}\right)+\alpha_L\rho_L\Pi_{\boldsymbol{\varepsilon},L} \tag{4}$$

where $C_{1\varepsilon}$, $C_{2\varepsilon}$, σ_k, σ_ε and C_μ are the model constants, and set as 1.42, 1.68, 1.0 and 1.3, 0.0845, respectively. $G_{k,L}$ represents the generation of turbulent kinetic energy due to the mean velocity gradients. $\mu_{m,L}$ represent the molecular viscosity of liquid phase.

On the right-hand side of Eqs. (3) and (4), $\Pi_{k,L}$ and $\Pi_{\varepsilon,L}$ are the source terms due to bubble induced turbulence, and determined by Troshko and Hassan [36]:

$$\Pi_{k,L}=0.75\frac{K_{GL}}{\alpha_L\rho_L}|\boldsymbol{u}_G-\boldsymbol{u}_L|^2 \tag{5}$$

$$\Pi_{\varepsilon,L}=0.45\frac{3C_D|\boldsymbol{u}_G-\boldsymbol{u}_L|}{2C_{VM}d_B}\Pi_{k,L} \tag{6}$$

where K_{GL} represent the covariance of the velocities of the continuous and the dispersed phases. C_{VM} is the virtual mass coefficient and C_D is the drag force coefficient.

2.3. Population balance model

The PBM is widely used to simulate the evolutions of bubble size distributions in bubble columns. The population balance equation is presented as follows:

$$\begin{aligned}\frac{\partial n(V,t)}{\partial t}+\nabla\cdot[\boldsymbol{u}_G\cdot n(V,t)]+\nabla_V\cdot[G_V n(V,t)]&=\frac{1}{2}\int_0^v c(V-V',V')n(V-V',t)n(V',t)\mathrm{d}V'\\&-\int_0^\infty c(V,V')n(V,t)n(V',t)\mathrm{d}V'\\&+\int_v^\infty pb(V')\beta(V,V')n(V',t)\mathrm{d}V'-b(V)n(V,t)\end{aligned} \tag{7}$$

where $n(V,t)$ represents the number density of bubbles of volume V per unit flow field space. The coalescence rates $c(V,V')$, the breakup rates $b(V')$ and the daughter size distribution $\beta(V,V')$ are solved by bubble coalescence–breakup models.

In the third term on the left-hand side of Eq. (7), G_V represents the volume-based growth rate of bubble volume due to interfacial mass transfer between the gas and liquid phases, which is discussed in next section.

The collision frequency between bubbles $\omega_{c,ij}$ and the product of the coalescence efficiency $P_{c,ij}$ are modeled by Varallo *et.al.* [37]:

$$\omega_{c,ij}=0.16\frac{0.8}{0.8-\alpha_G}\left[1-\exp\left(-3\frac{0.928\alpha_G^{1/3}}{0.928-\alpha_G^{1/3}}\right)\right]\left(d_i+d_j\right)^2\varepsilon^{1/3}\left(d_i^{2/3}+d_j^{2/3}\right)^{1/2} \tag{8}$$

$$P_{c,ij}=min\left(1,\frac{0.08}{\sqrt{2}\varepsilon^{1/3}\left(d_i^{2/3}+d_j^{2/3}\right)^{1/2}}\right) \tag{9}$$

where d_i and d_j represent the bubble diameter of i-th and j-th bubbles, respectively.

For breakup model, a new model developed by the authors group [38] is used to compute the overall breakup frequency of bubbles $b(d)$ and the daughter size distribution $\beta(d,f_v)$:

$$b(d)=c(1-\alpha_G)n\left(\frac{\varepsilon}{d^2}\right)^{1/3}\int_{\frac{11.4\eta}{d}}^1\frac{(1+\xi)^2}{\xi^{11/3}}\cdot\exp\left[-\max\left(\frac{\sigma}{2\rho_L d^{5/3}\varepsilon^{2/3}\xi^{2/3}},\frac{12\sigma\xi^{4/3}}{\pi^2\rho_L d^{5/3}\varepsilon^{2/3}}\right)\right]\mathrm{d}\xi \tag{10}$$

$$\beta(d,f_v)=\frac{b(d,\xi)}{b(d)}\cdot\left[\frac{1}{3}\left(f_v^{-1}-1\right)^{-4/3}f_v^{-2}\right] \tag{11}$$

where d is the diameter of the mother bubble. η is Kolmogorov length scale. ξ is dimensionless eddy scale. f_v is fragmentation ratio. In this simulation, the population balance model is discretized using 13 bubble size classes. This number was selected to achieve an optimal balance between numerical accuracy and computational expense, which has been proven in our previous work [38].

2.4. Interphase mass transfer

The mass transport is described by the continuity equations of species:

$$\frac{\partial\left(\alpha_q\rho_q Y_q^s\right)}{\partial t}+\nabla\cdot\left(\alpha_q\rho_q\boldsymbol{u}_q Y_q^s\right)=\nabla\cdot\left[\left(D_q^s+\frac{\mu_{t,q}}{\rho_q Sc_q}\right)\alpha_q\rho_q\nabla Y_q^s\right]+\dot{m}_q^s \tag{12}$$

where Y_q^s, D_q^s and $\dot{m}_q^s$ are the mass fraction, the molecular diffusion coefficients and the mass source of CO_2 in phase q, respectively.

The PBM is solved by the discrete method and represents the continuous bubble size distribution in terms of a set of discrete size classes. Accordingly, the interfacial mass transfer source $\dot{m}_q^s$ is a summation of the interfacial mass transfer rate of each bubble class, defined as

$$\dot{m}_L^{CO_2}=-\dot{m}_G^{CO_2}=-\rho_G^{CO_2}\sum_{i=1}^N G_{V,i}n_i \tag{13}$$

Table 2
Summary of mass transfer models.

Mass transfer models	Correlations of k_L
Ranz–Marshall [14]	$k_L = \frac{D_L}{d_B}(2+0.6Re^{1/2}Sc^{1/3})$
Brauer [15]	$k_L = \frac{D_L}{d_B}(2+0.015Re^{0.89}Sc^{0.7})$
Higbie [16]	$k_L = 2\sqrt{\frac{D_L U_{slip}}{\pi d_B}}$
Bird [17]	$k_L = 2\sqrt{\frac{D_L U_{slip}}{3\pi d_B}}$
Kawase [20]	$k_L = 1.13(\varepsilon\nu)^{1/4}Sc^{-1/2}$

Table 3
Physical properties of the gas and liquid phases.

Material	ρ/kg·m^{-3}	μ/Pa·s	σ/N·m^{-1}	He^{CO_2}	D^{CO_2}/m^2·s^{-1}	Sc_L
CO_2	1.850	1.440×10^{-5}	0.073	1.043	1.460×10^{-9}	–
Air	1.230	1.780×10^{-5}	–	–	–	–
H_2O	998.200	1.160×10^{-3}	–	–	–	795.950

where n represents the amount of bubble classes, i represents the index of specific bubble class, ranging from 1 to N. $G_{V,i}$ is the volume-based growth rate of specific bubble class. Neglecting the mass transfer resistance in gas phase, the interphase mass transfer rate of carbon dioxide is calculated as follows:

$$G_{V,i} = \frac{k_L a_i}{n_i}\frac{\left(He^{CO_2}Y_G^{CO_2}\rho_G - Y_L^{CO_2}\rho_L\right)}{\rho_G^{CO_2}} \tag{14}$$

where He^{CO_2} is the Henry constant for carbon dioxide, $Y_G^{CO_2}$ and $\dot{m}_G^{CO_2}$ are the mass fraction and the mass source of carbon dioxide in gas phase, respectively. $Y_L^{CO_2}$ and $\dot{m}_L^{CO_2}$ are the mass fraction and the mass source of carbon dioxide in liquid phase, respectively. n_i is the number density of specific bubble class. Following Versteeg & van Swaaij [39], He^{CO_2} is computed by:

$$He^{CO_2} = 3.54\times10^{-7}RT\exp\left(\frac{2044}{T}\right) \tag{15}$$

where R is the universal gas constant. T is the operating temperature. k_L is the mass transfer coefficient of the liquid phase. a is the interfacial area concentration and defined as:

$$a = \frac{6\alpha_G}{d_B} \tag{16}$$

where d_B is mean bubble diameter, which is solved by PBM.

For the simulations of absorption or desorption of carbon dioxide in water, five models (listed in Table 2) were selected for comparison, including the single bubble-based models [14,15], the slip velocity models [16,17], and the eddy cell model [20]. Note that the slip velocity U_{slip} shown in Table 2 is defined as $U_{slip} = |\boldsymbol{u}_G - \boldsymbol{u}_L|$ [28].

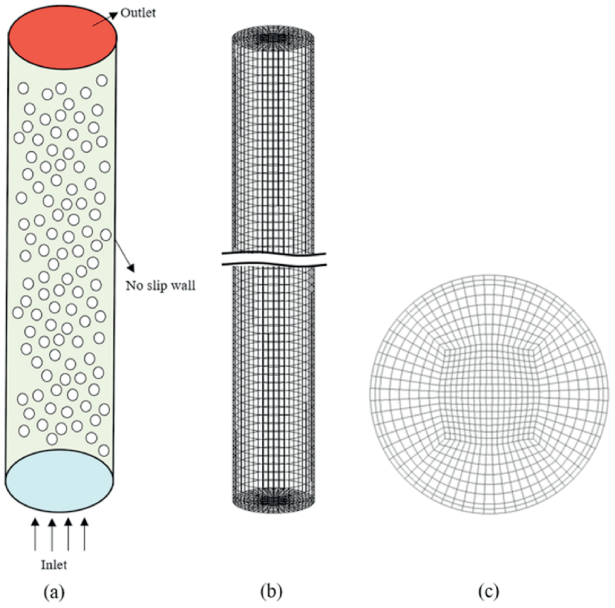

Fig. 1. Computational domain: (a) geometric schematic, (b) 3D mesh structure, and (c) radial distribution of mesh.

2.5. The benchmark simulation cases

In present work, the benchmark simulation cases are set up based on the experiments of Deckwer *et al.* [29]. The experimental facility was a 7.2 m high and 0.2 m internal diameter cylindrical bubble column. A mixture of air and carbon dioxide was used. The bubble column was operated at temperature of 14 °C and filled with water up to 7.2 m. The physical properties of the gas and liquid phases are listed in Table 3. Five sets of operating conditions, including co-current flow, counter-current flow, were selected and summarized in Table 4. Of noting, cases 1–5 correspond to W23, W6, W13, W15 and W16 of Deckwer *et al.* [29], respectively. Case 5 is solely used to compare the effects of different operating modes on gas–liquid mass transfer and is not employed to discuss the applicability of the mass transfer model. The measurement data including the time-averaged gas holdup and the mass fraction of carbon dioxide were used for comparison.

3D numerical simulations were conducted by using ANSYS Fluent. The geometric diagram and meshes were shown in Fig. 1. A full 3D geometry is used in simulation. For the boundary conditions, the bottom and top of the bubble column were set as velocity inlet and pressure outlet, respectively. The gas and liquid were input uniformly through the entire bottom as shown in Fig. 1(a). The

Table 4
Summary of experimental data from Deckwer *et al.* [29].

Case	Operation mode	Superficial gas velocity, J_G/m·s^{-1}	Superficial liquid velocity, J_L/m·s^{-1}	CO_2 mass fraction in gas phase, $Y_G^{CO_2}$ (bottom)	CO_2 mass fraction in liquid phase, $Y_L^{CO_2}$ (top/bottom)	Pressure at outlet / kPa
1	Co-current	0.0261	0.0265	0.493	0 (bottom)	105.9
2		0.0050	0.0265	0	0.001630 (bottom)	104.3
3	Counter-current	0.0144	−0.0265	0.818	0.000300 (top)	101.9
4		0.0196	−0.0265	0.660	0.000285 (top)	102.3
5		0.0258	−0.0265	0.527	0.000295 (top)	104.0

initial phase velocities of gas and liquid at the inlet were determined by $u_G = J_G/\alpha_G$ and $u_L = J_L/\alpha_L$, respectively, which is a conventional approach in the simulations of Deckwer experiment (*e.g.*, Rzehak and Krepper [9], Li *et al.* [28]). In a simulation, the initial gas volume fraction at the inlet was set as 0.001, and the initial volume fraction of liquid at the inlet was calculated by $\alpha_L = 1 - \alpha_G$. In co-current mode, gas and liquid flow in same positive direction, and the velocities were set positive at the inlet. In counter-current mode, the liquid velocity was set negative and the gas was set positive. The outlet pressure of each case was set according to the experiment data listed in Table 4. In Deckwer's experimental setup, the bubble column was equipped with a gas sparger consisting of 56 cross-distributed nozzles, each with a 1 mm diameter. Due to the challenge of resolving such fine geometric features in the computational mesh, a simplified uniform inlet was adopted instead. Since the initial diameter at the inlet was not reported, it is calculated by the empirical correlation developed by Polli *et al.* [40], which is specifically recommended for this type of distributor. This correlation is widely adopted in CFD simulations of bubble columns to estimate the initial bubble size generated by multi-nozzle spargers. And the initial bubble diameters were calculated as 9.6, 5.6, 7.9, 8.8, and 9.6 mm for cases 1–5, respectively. The gas phase was treated as ideal gas and the liquid phase was considered as incompressible. The wall was set to no-slip wall boundary. As for the near-wall resolution, a strategy of moderate mesh refinement near the wall to balance computational cost with numerical accuracy, which has been proven in our previous work [38].

The second order upwind discretization scheme was employed for momentum, turbulent, and species transport equations, and the QUICK scheme was adopted for the volume fraction equation. The convergence criteria for all equations were set to residuals below 1×10^{-4} per iteration. The time step for transient simulations was 0.005 s. An initial transient development required approximately 500 s to reach a quasi-steady state, as indicated by the stabilization of key parameters (*e.g.*, volume-averaged gas holdup and species concentration) and consistently meeting the residual criteria. The computation was then continued for an additional 500 s to collect sufficient data for statistically steady time-averaged results of distributions of gas holdup, species mass fraction, *etc*. The attainment of statistical convergence was confirmed by monitoring the temporal evolution of these volume-averaged parameters over the final 500 s, ensuring negligible fluctuations.

3. Results and Discussion

3.1. Grid independence study

Given the need to employ five distinct models across five simulation cases, conducting a grid independence study with three different mesh resolutions (6000, 25000 and 79000) would entail a prohibitively high computational cost. Therefore, it was necessary to first identify the most suitable model and perform grid independence study under only one representative condition (case 1). The Kawase model was selected for this purpose, as it is not only theoretically the most comprehensive but was also validated in our subsequent simulations. As shown in Fig. 2, the axial profiles of simulated gas holdup and CO_2 mass fraction are compared against experimental measurements from Deckwer *et al.* [29]. The observed variations in gas holdup near the inlet region across different meshes are primarily attributed to simplifications in the inlet boundary condition. It should be noted that, despite these local discrepancies near the inlet, the key global parameters—such as the total gas holdup and the mass transfer coefficient—exhibit strong mesh independence. This indicates that the local inlet simplification has negligible influence on the overall simulation outcomes. The average deviations between the simulation results and experimental data for different meshes (6000, 25000, and 79000 cells) are as follows. For gas holdup, the deviations were 10.69%, 4.56%, and 4.46%, respectively. For the CO_2 mass fraction in the gas phase, the corresponding average deviations were 9.64%, 9.11%, and 8.98%, respectively. Consequently, the 25000 mesh resolution was adopted for all subsequent simulations, achieving an optimal balance between numerical accuracy and computational cost.

3.2. Co-current flow

Fig. 3 shows the simulated gas holdup and the CO_2 mass fraction in gas phase, respectively. The experimental data of co-current absorption case 1 are also shown in the same figure for comparisons with the simulation results by using different mass transfer models. Comparing the simulation results with experimental data, it is observed that the mass transfer rate predicted by Ranz–Marshall model is underestimated, resulting in an overestimation of the gas holdup and CO_2 mass fraction in gas phase. This is because the Ranz–Marshall model is primarily based on single-bubble mass transfer theory and rely on parameters such as bubble diameter, slip velocity, and Reynolds number (*Re*). Consequently, it fails to adequately represent the behavior of bubble swarms or capture the influence of turbulence on interphase mass transfer. On the other side, the simulation results for Kawase model agree with the experimental data in terms of the gas holdup and CO_2 mass fraction. Comparing with other models, Higbie, Bird and Brauer model underestimates mass transfer in the bottom half of a bubble column. In addition, all mass transfer models accurately predicted the gas holdups in the inlet section, even though the geometry of the bubble column inlet was simplified.

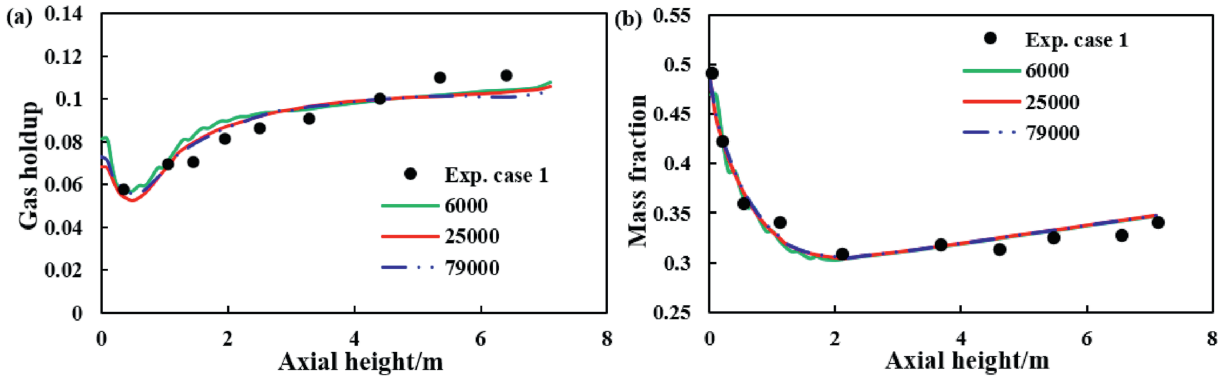

Fig. 2. Comparisons of simulation results of case 1 using different meshes: (a) cross-sectional area averaged gas holdup along the height of bubble column, and (b) cross-sectional area averaged mass fraction along the height of bubble column.

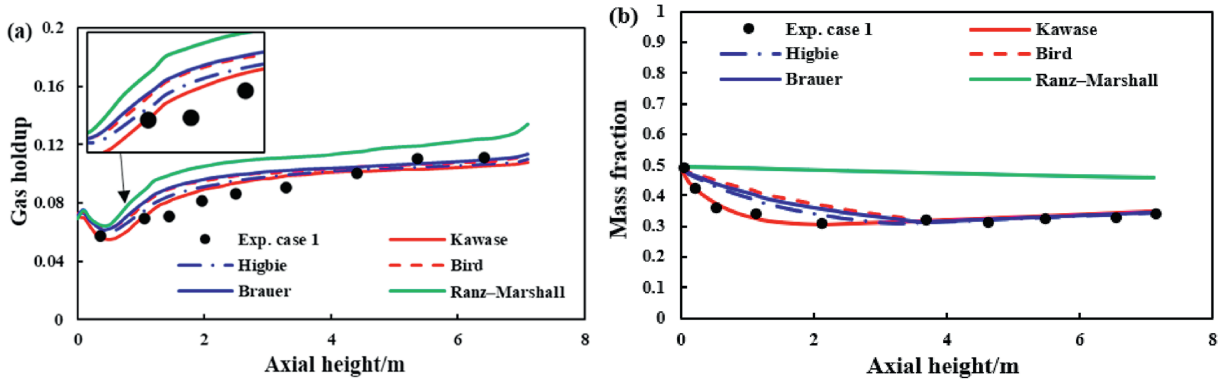

Fig. 3. Comparisons between simulated results and experimental data (case 1): (a) gas holdup, and (b) CO_2 mass fraction in gas phase.

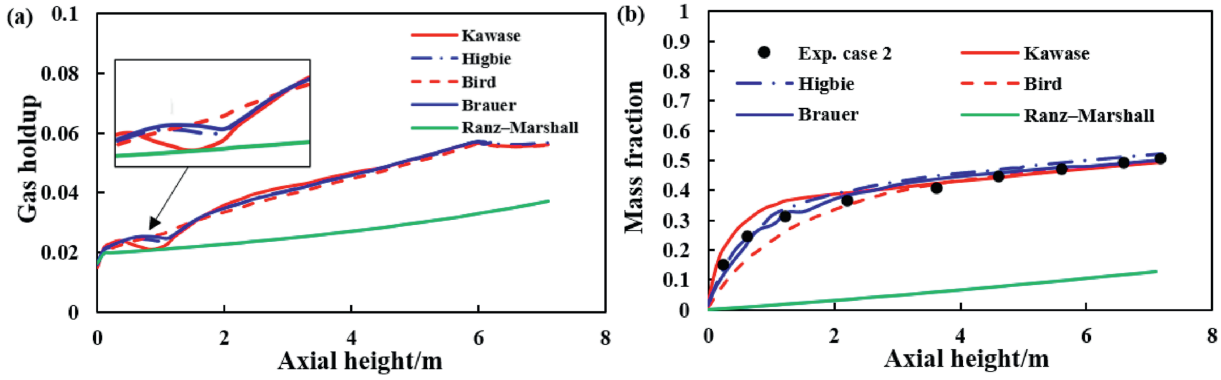

Fig. 4. Comparisons between simulated results and experimental data (case 2): (a) gas holdup, and (b) CO_2 mass fraction in gas phase.

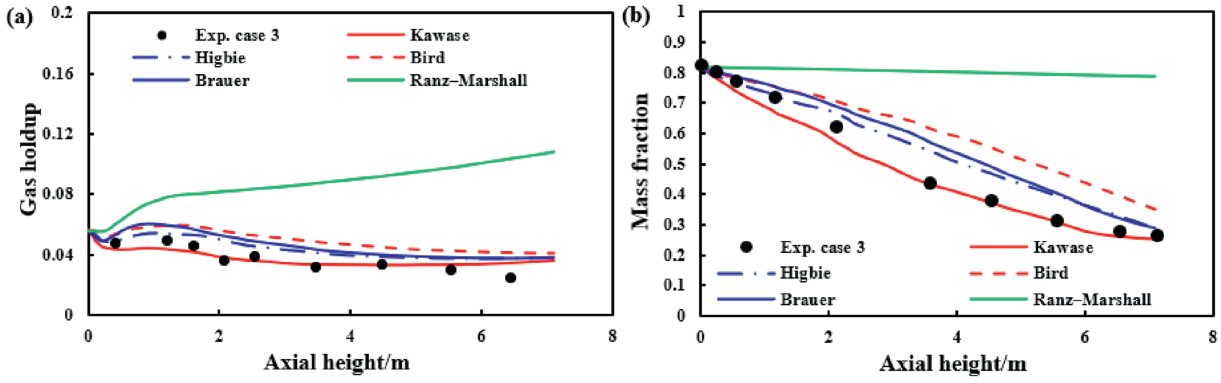

Fig. 5. Comparisons between simulated results and experimental data (case 3): (a) gas holdup, and (b) CO_2 mass fraction in gas phase.

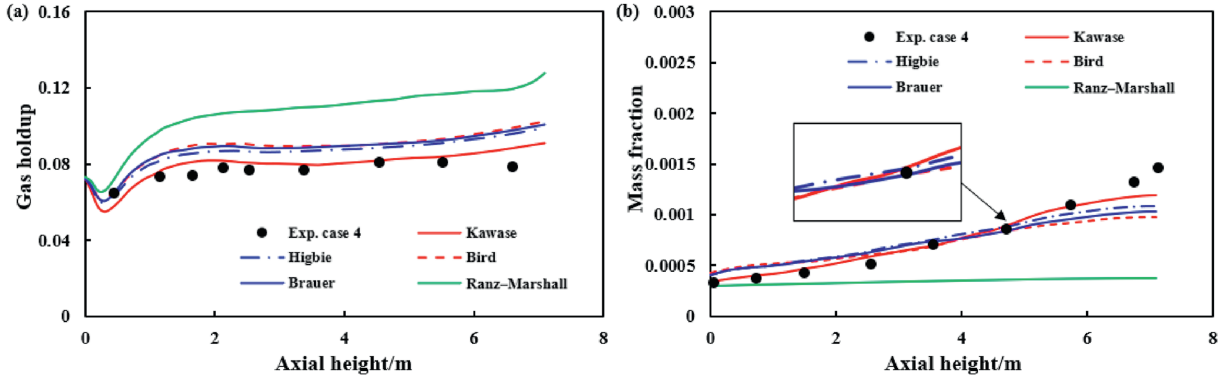

Fig. 6. Comparisons between simulated results and experimental data (case 4): (a) gas holdup, and (b) CO_2 mass fraction in liquid phase.

Table 5
Comparisons between volume-averaged mass transfer coefficients calculated by different mass transfer models and experimental data ($m \cdot s^{-1}$).

Case	Exp. data	Kawase	Higbie	Bird	Brauer	Ranz–Marshall
1	9.06×10^{-5}	7.50×10^{-5}	2.62×10^{-5}	1.33×10^{-5}	1.66×10^{-5}	5.03×10^{-6}
2	1.10×10^{-4}	1.31×10^{-4}	4.46×10^{-4}	3.06×10^{-4}	3.43×10^{-4}	7.07×10^{-6}
3	8.91×10^{-5}	7.95×10^{-5}	2.75×10^{-5}	1.71×10^{-5}	1.97×10^{-5}	5.80×10^{-6}
4	9.35×10^{-5}	8.44×10^{-5}	2.98×10^{-5}	1.80×10^{-5}	2.17×10^{-5}	5.42×10^{-6}

For co-current desorption, case 2 was used to verify the simulation results. Herein, the gas and liquid phases entered the bubble column at different speeds and flowed upwards simultaneously. Before entering the bubble column, a certain concentration of carbon dioxide was dissolved in the liquid phase, while only air was present in the gas phase. As shown in Fig. 4, after being resolved through the gas–liquid interface, carbon dioxide in the liquid phase mixed with air, which results in increases in the gas holdup and the mass fraction of carbon dioxide in gas phase along the axial height of bubble column. Fig. 4(a) shows the predicted gas holdup distributions by using different mass transfer models, and Fig. 4(b) shows the predicted mass fraction of carbon dioxide in gas phase. The experimental data of gas holdup were not found and only the mass fraction of CO_2 in gas phase were reported in Deckwer *et al.* [29] were indicated in Fig. 4(b) for comparison. The Ranz–Marshall model underestimates mass transfer significantly. The Kawase model slightly overestimate CO_2 mass fraction, Bird model overestimates CO_2 mass fraction, and Higbie and Brauer models show better agreements with experimental data.

3.3. Counter-current flow

This section presents a comparative analysis of simulation results for counter-current gas absorption (cases 3 and 4) using

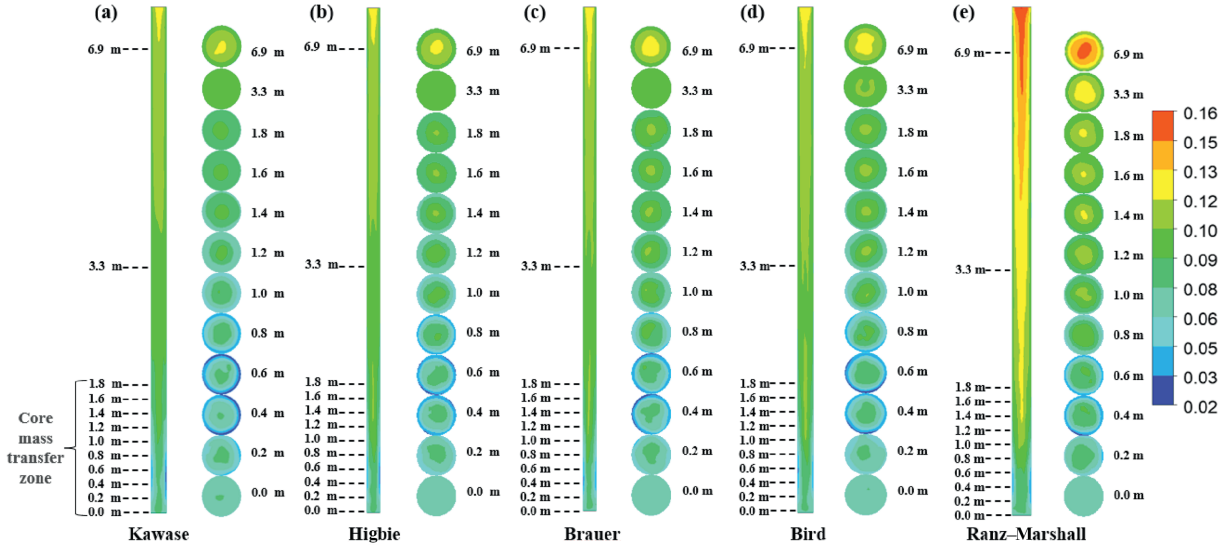

Fig. 7. Contours of simulated gas holdup with (a) Kawase, (b) Higbie, (c) Brauer, (d) Bird, and (e) Ranz–Marshall models for case 1.

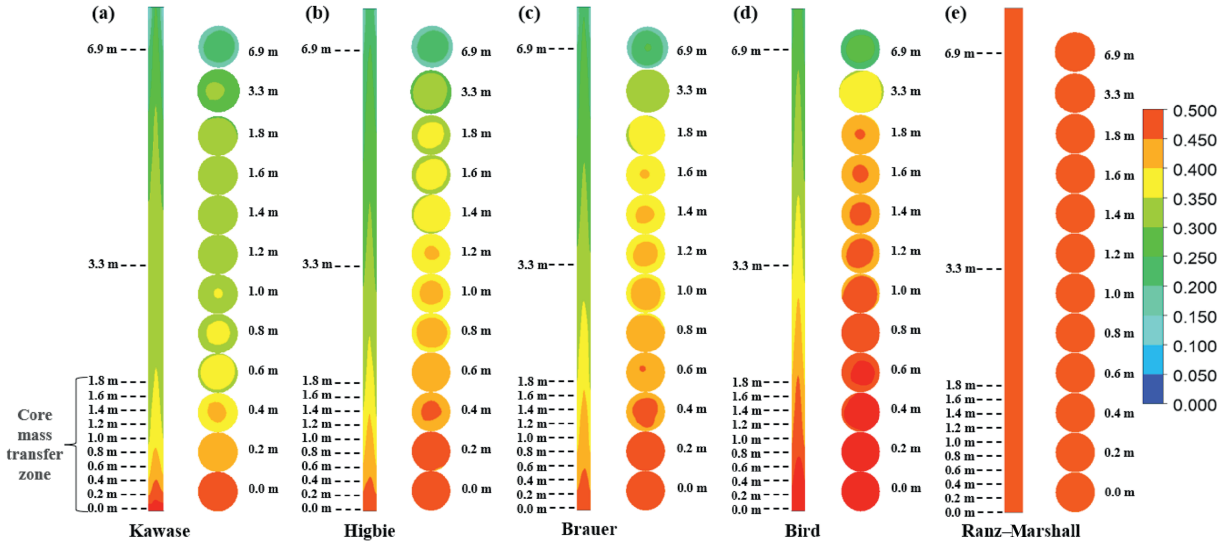

Fig. 8. Contours of simulated CO_2 mass fraction in gas phase with (a) Kawase, (b) Higbie, (c) Brauer, (d) Bird, and (e) Ranz–Marshall models for case 1.

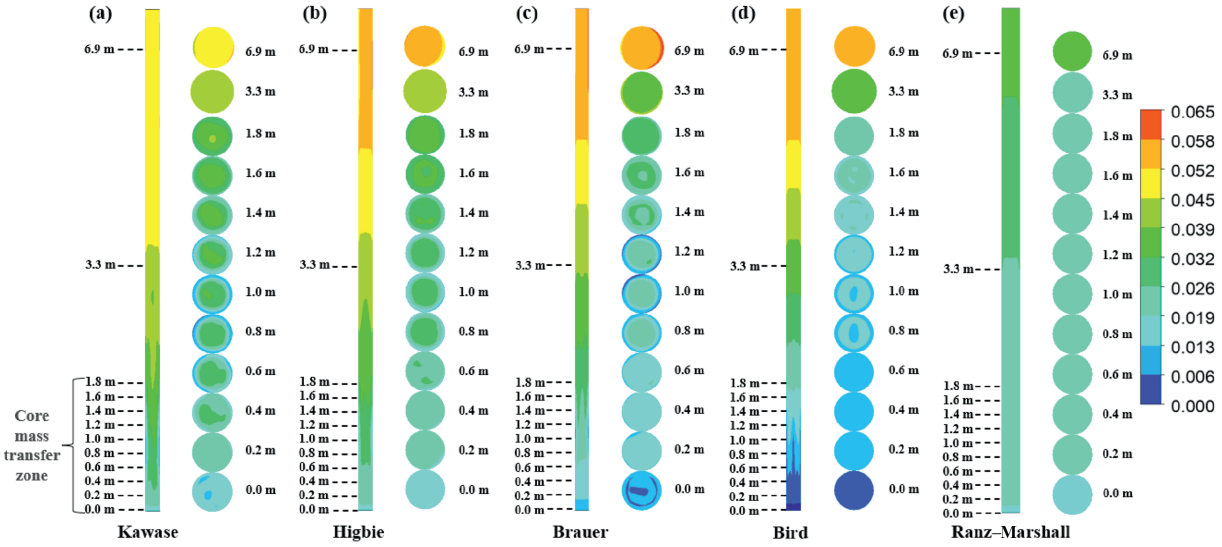

Fig. 9. Contours of simulated gas holdup with (a) Kawase, (b) Higbie, (c) Brauer, (d) Bird, and (e) Ranz–Marshall models for case 2.

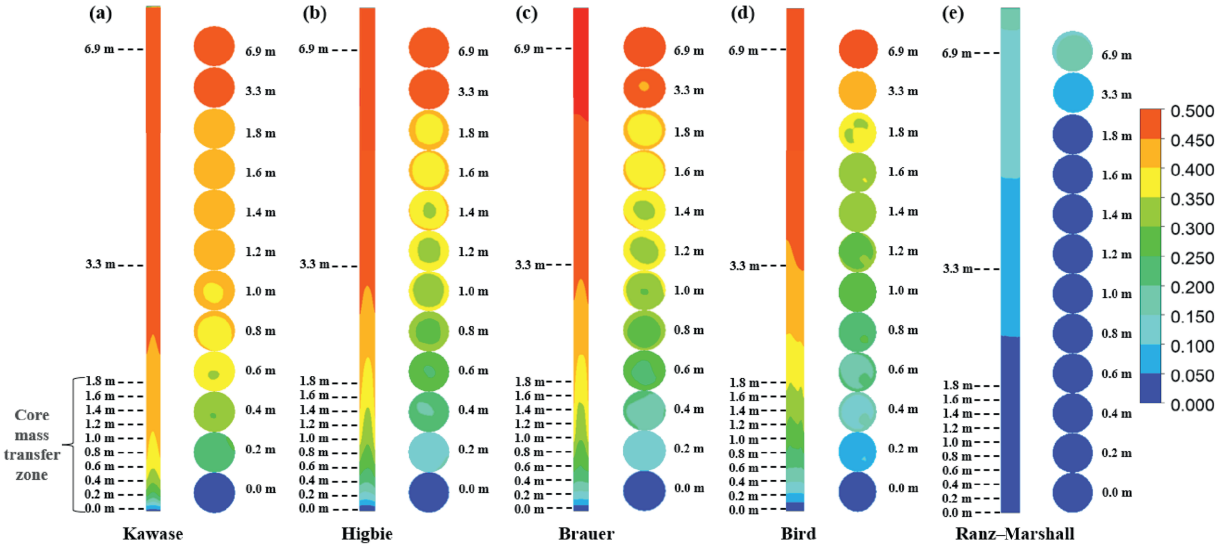

Fig. 10. Contours of simulated CO_2 mass fraction in gas phase with (a) Kawase, (b) Higbie, (c) Brauer, (d) Bird, and (e) Ranz–Marshall models for case 2.

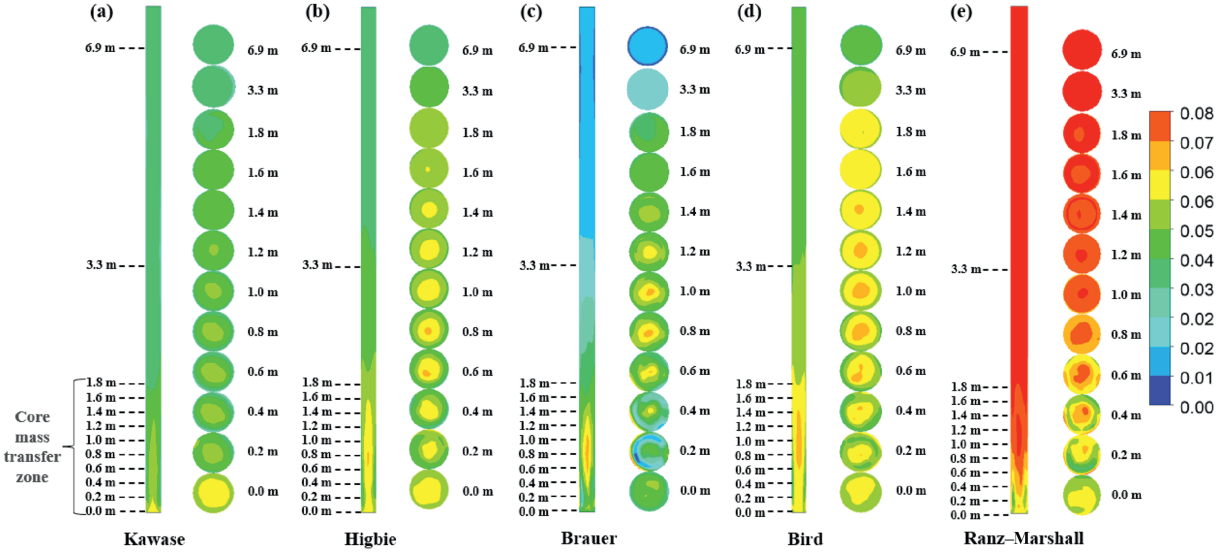

Fig. 11. Contours of simulated gas holdup with (a) Kawase, (b) Higbie, (c) Brauer, (d) Bird, and (e) Ranz–Marshall models for case 3.

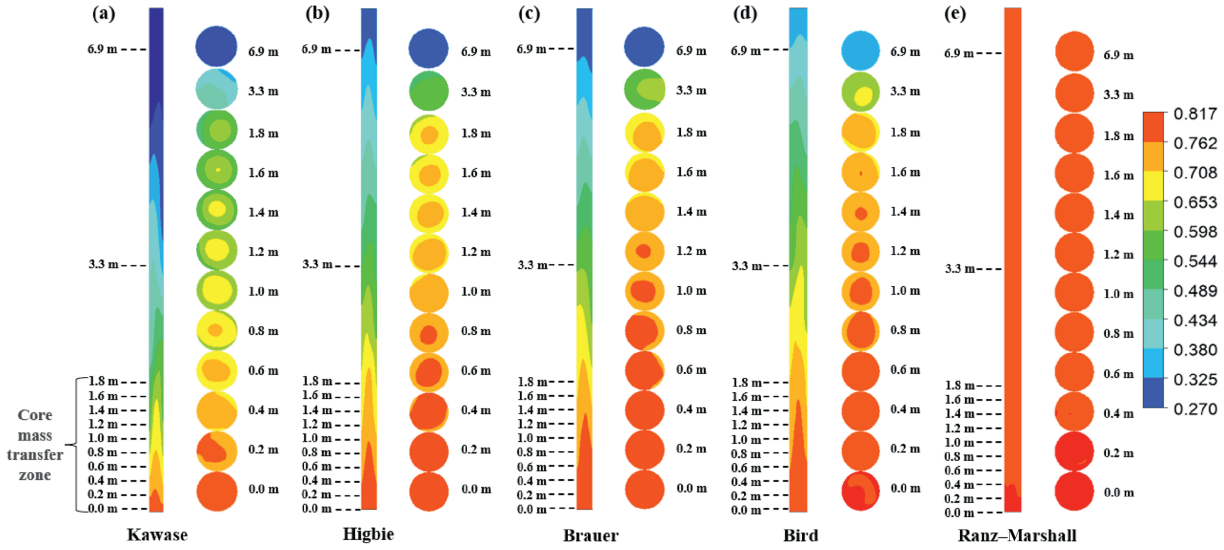

Fig. 12. Contours of simulated CO_2 mass fraction in gas phase with (a) Kawase, (b) Higbie, (c) Brauer, (d) Bird, and (e) Ranz–Marshall models for case 3.

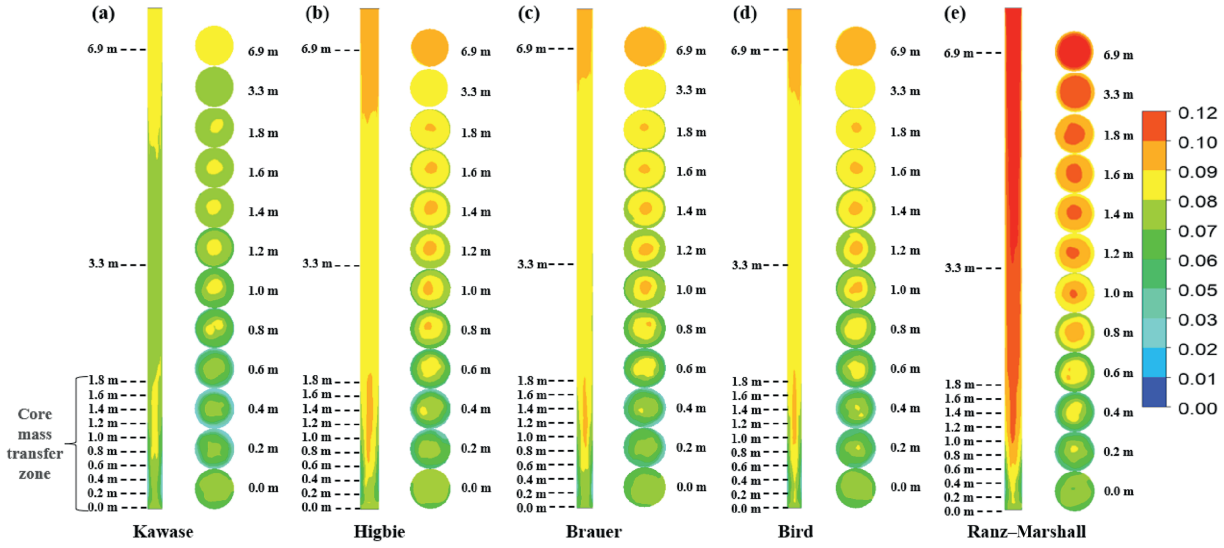

Fig. 13. Contours of simulated gas holdup with (a) Kawase, (b) Higbie, (c) Brauer, (d) Bird, and (e) Ranz–Marshall models for case 4.

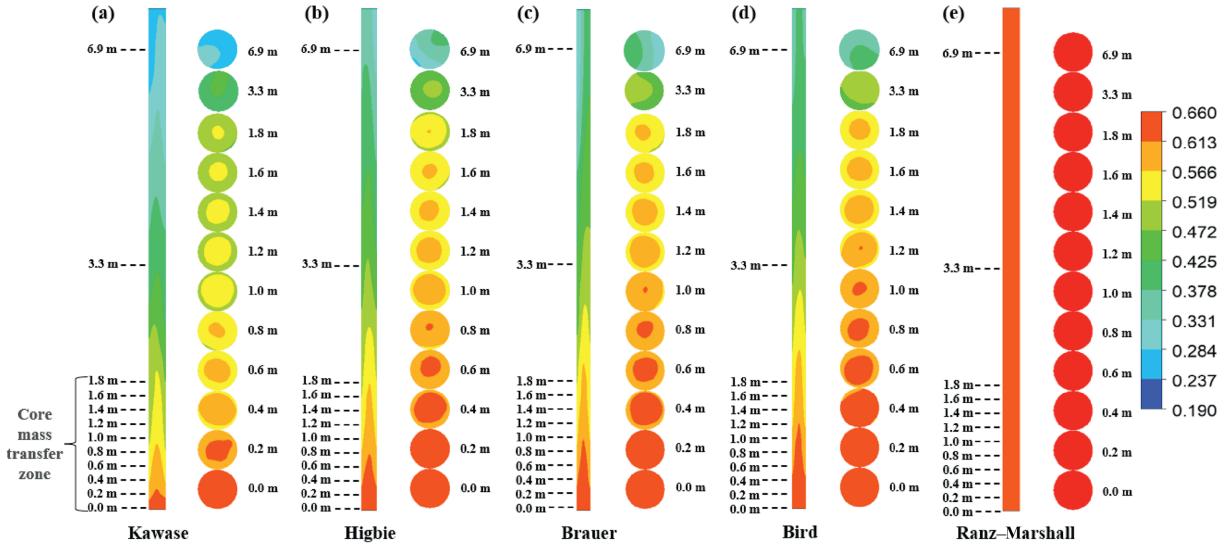

Fig. 14. Contours of simulated CO_2 mass fraction in gas phase with (a) Kawase, (b) Higbie, (c) Brauer, (d) Bird, and (e) Ranz–Marshall models for case 4.

Table 6
Comparison of experimental and simulated bubble sizes (mm).

Case	Exp. data	Model simulation results				
		Kawase	Higbie	Bird	Bruaer	Ranz–Marshall
1	2.93	3.05	2.99	2.89	3.01	2.89
2	3.20	3.31	3.39	3.46	3.44	3.76
3	2.90	3.24	3.22	3.18	3.13	3.15
4	3.01	3.08	3.07	3.06	3.08	2.90

different mass transfer models. The system consists of an upward-flowing gas phase (air/CO_2 mixture) entering from the column bottom and a downward-flowing liquid phase (water with dissolved CO_2) introduced at the top. To implement the counter-current flow configuration, the liquid phase velocity was specified as a negative value in the boundary conditions. Figs. 5 and 6 compare the model predictions, with subplots (a) displaying the axial gas holdup distributions and subplots (b) showing the vertical profiles of CO_2 mass fraction in both gas and liquid phases, respectively.

Figs. 5 and 6 demonstrate that the Kawase model provides satisfactory agreement with experimental data for counter-current gas absorption, exhibiting strong potential for accurate mass transfer predictions in complex flow regimes. While the Higbie, Bird, and Brauer models successfully capture the qualitative trends in axial distributions, quantitative discrepancies with experimental measurements remain evident. Notably, the Ranz–Marshall model consistently underestimates mass transfer rates while producing anomalously high predictions for both gas holdup and CO_2 mass fraction in the gas phase.

Table 5 presents the comparison between the predicted mass transfer coefficients by various models and the experimental values. It highlights the performance of the Kawase model in predicting the mass transfer coefficient across all cases.

Notably, the Ranz–Marshall model and the Brauer model are similar in their mathematical form, but differ in the exponents applied to the *Re* and Schmidt number (*Sc*). It is therefore predictable that their computational results would differ. In fact, the Ranz–Marshall model is a classical empirical correlation developed for mass transfer from rigid spheres in uncontaminated

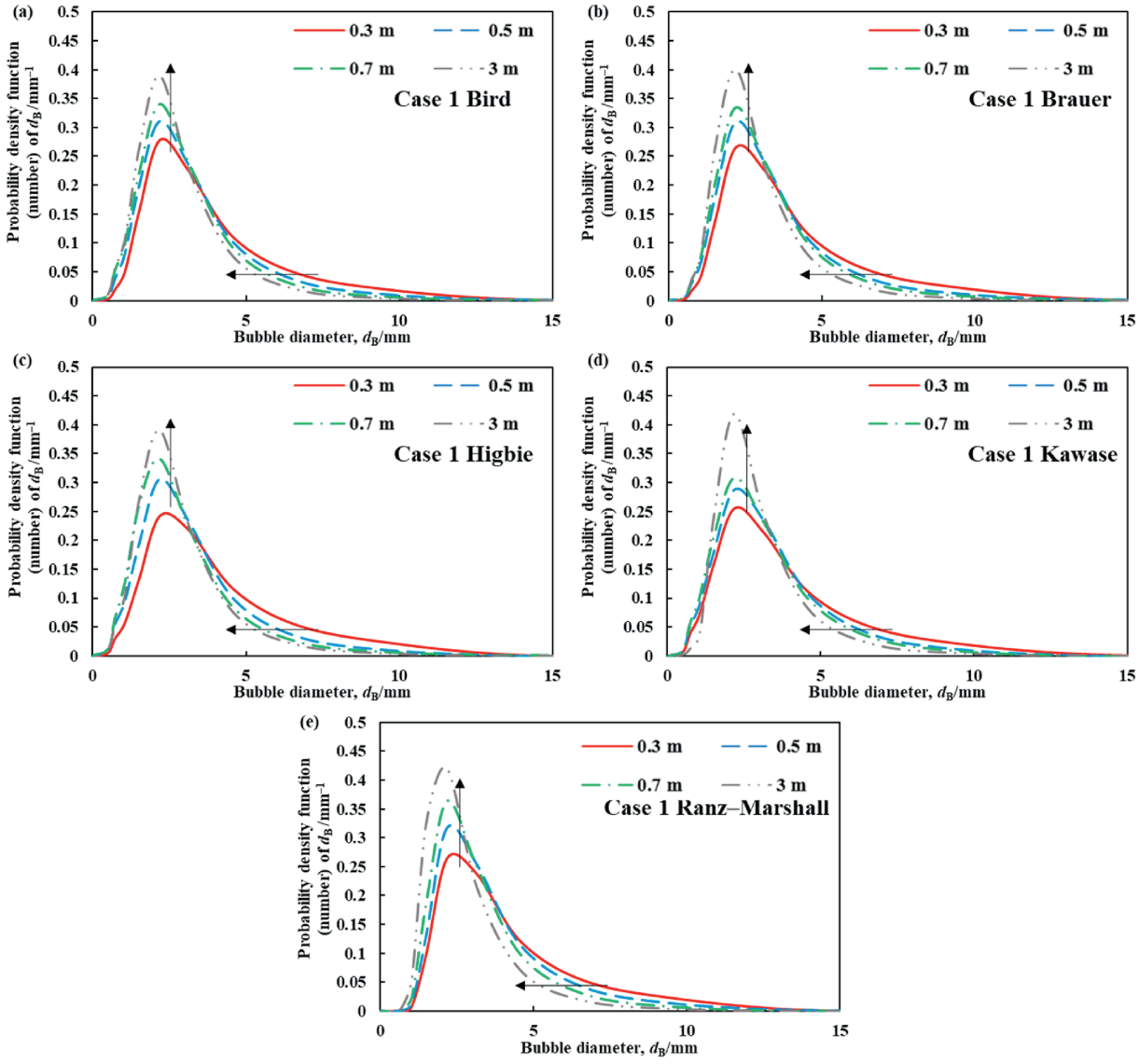

Fig. 15. Bubble sizes distributions at different heights with various mass transfer models: (a) Bird, (b) Brauer, (c) Higbie, (d) Kawase, and (e) Ranz–Marshall for case 1.

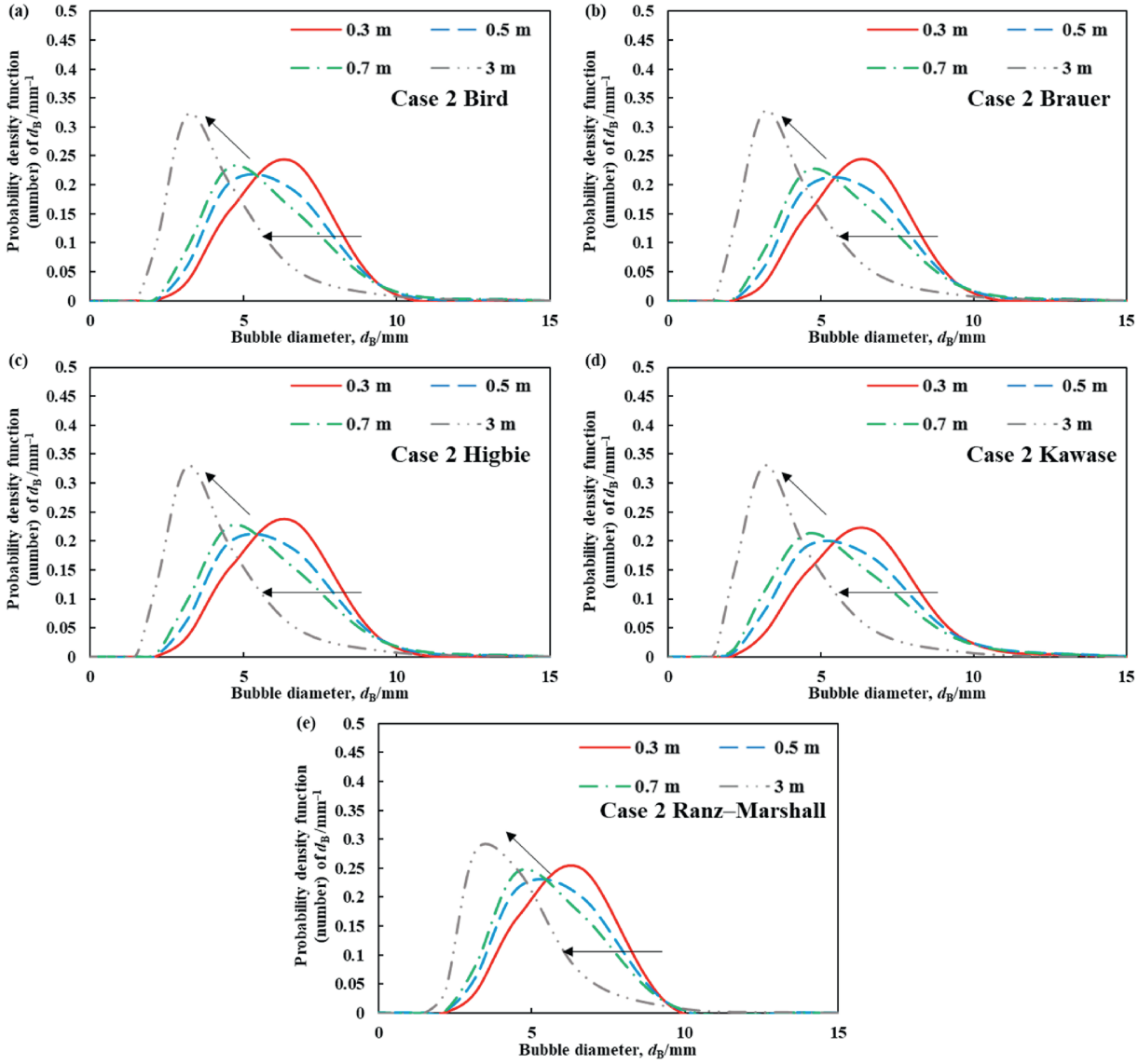

Fig. 16. Bubble size distributions at different heights with various mass transfer models: (a) Bird, (b) Brauer, (c) Higbie, (d) Kawase, and (e) Ranz–Marshall for case 2.

flows, whereas the Brauer model was specifically designed for gas–liquid systems and incorporates relevant mechanisms for bubble column simulations, such as dependencies on bubble diameter and liquid properties. These fundamental differences explain the divergence in their exponent values.

In addition, the Higbie and Bird models are mathematically similar, sharing identical exponents for the *Re* and *Sc*, as both are derived from the same underlying physical principle. Consequently, their simulation results are close. Similarly, the Lamont–Scott model [19] (another eddy cell model) is mathematically analogous to the Kawase model, also sharing identical exponents, but differs primarily in the predicted mass transfer coefficients—the Lamont–Scott value being approximately one-third of that predicted by the Kawase model. By analogy with the similarity between the Higbie and Bird models, which are also mathematically consistent, it is expected that the Kawase and Lamont–Scott models would exhibit identical trends. Since the current results show that the Kawase model agrees best with the experimental data among all the models tested, it can be reasonably inferred that the Lamont–Scott model would significantly underpredict mass transfer under the present conditions. Additional simulations comparing the Lamont–Scott and Kawase models for representative cases (cases 1 and 3) were also conducted. The results, provided in Supplementary Material S1, confirm that the Kawase model remains the best-performing one, while the Lamont–Scott model consistently underestimates key parameters—consistent with the difference in model constants.

3.4. Contours of simulation results with different mass transfer model

Figs. 7–14 present a comprehensive comparison of axial and radial distributions for gas holdup and CO_2 mass fraction across cases 1–4 using different mass transfer models. The simulations reveal significant flow non-uniformity within the entrance region (0–1.8 m), particularly for gas holdup, where strong vortical oscillations occur due to inlet effects. Beyond 2 m height, the flow becomes more fully developed, exhibiting improved uniformity. All models predict similar radial profiles for CO_2 mass fraction, with peak concentrations at the column center that gradually decrease toward the walls. Comparative analysis shows case 2 achieves greater gas holdup uniformity than case 1 (seen in Fig. 9),

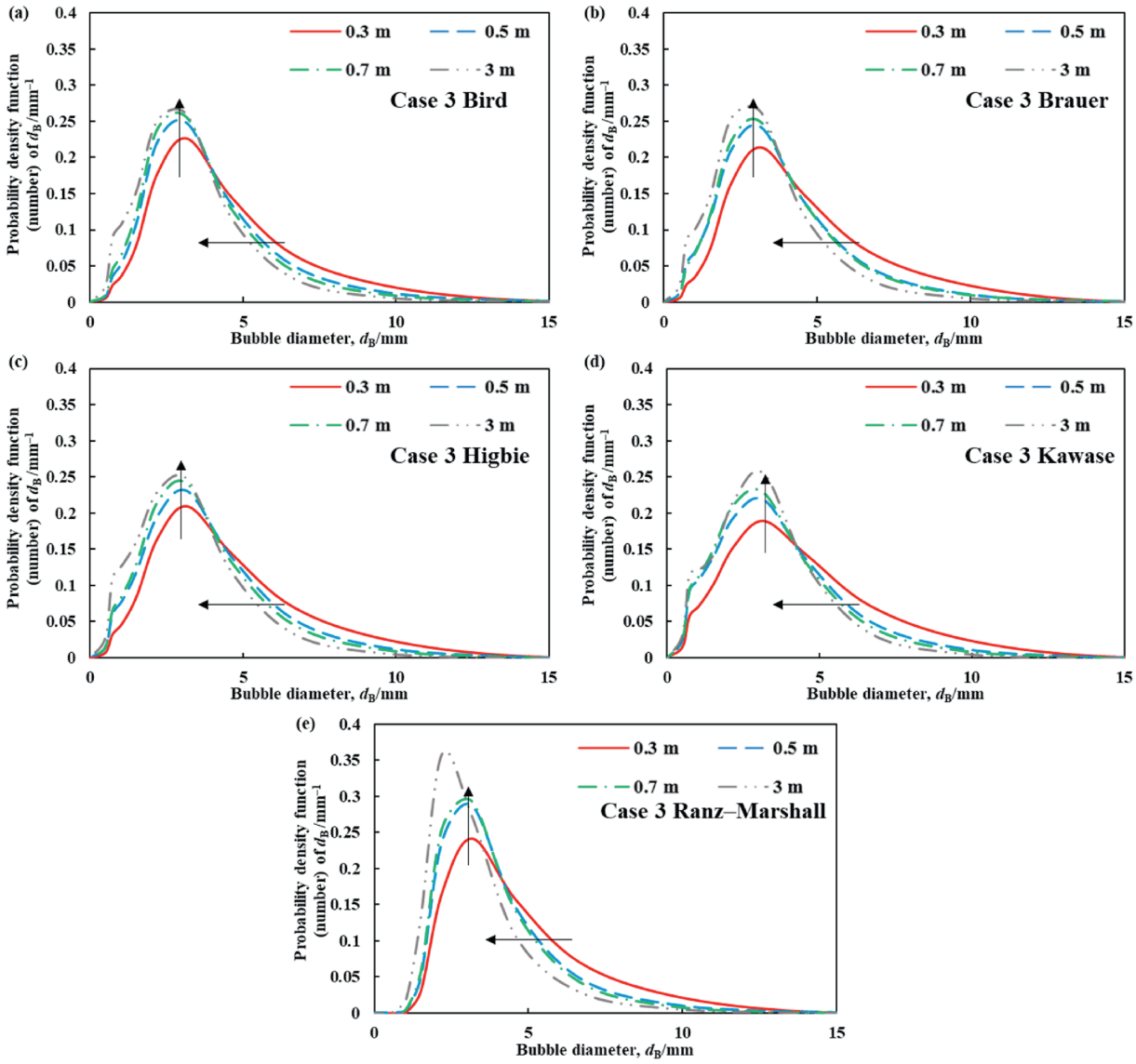

Fig. 17. Bubble size distributions at different heights with various mass transfer models: (a) Bird, (b) Brauer, (c) Higbie, (d) Kawase, and (e) Ranz–Marshall for case 3.

while counter-current flow demonstrates enhanced non-uniformity in the entrance region compared to co-current operation. This behavior stems from two key mechanisms: (1) the reverse flow configuration intensifies bubble coalescence and breakup dynamics, altering the bubble distribution patterns; and (2) the counter-current interaction reduces bubble rise velocities, leading to increased local gas holdup that amplifies distribution non-uniformity. These findings highlight the complex interaction between flow configuration, bubble dynamics, and mass transfer characteristics in bubble column reactors.

3.5. Bubble size distribution

Table 6 shows the comparison between bubble sizes calculated by different mass transfer models and experimental data. The simulated bubble sizes are close to the experimental data and the Kawase model gives the best results. Figs. 15–18 shows the distribution of bubble sizes at different heights for various mass transfer models for cases 1–4, respectively. The figures also indicate the d_{32} of the entire bubble column calculated by different models. In this simulation, only sectional data for bubble size distribution at heights of 0.3, 0.5, 0.7 and 3 m were collected, as the bubble size distribution remained largely unchanged after 3 m. The bubble size distribution predicted by different mass transfer models at various heights appears to be relatively consistent. Overall, the distribution of bubble sizes shifts towards smaller sizes with increasing height of the bubble column, indicating a trend towards reduced bubble sizes, the bubble size decreases as the height of the bubble column increases. Additionally, it was observed that the variation in bubble size distribution is more pronounced at heights of 0.3, 0.5, and 0.7 m. This indicates the presence of high-frequency bubble breakup and mass transfer near the entrance of the bubble column. After 3 m, the bubble size distribution remains relatively constant, indicating that the bubble size keeps stable. There are also some differences in the variation of bubble size distribution under different case. As the height of the bubble column increases, leading to different trends in the peak of the bubble size distribution across different scenarios. This may be attributed to the influences of various factors such as gas–liquid interactions, bubble coalescence and break-up behaviors, and gas–liquid mass transfer processes. These phenomena demonstrate the complexity and variability of gas–liquid

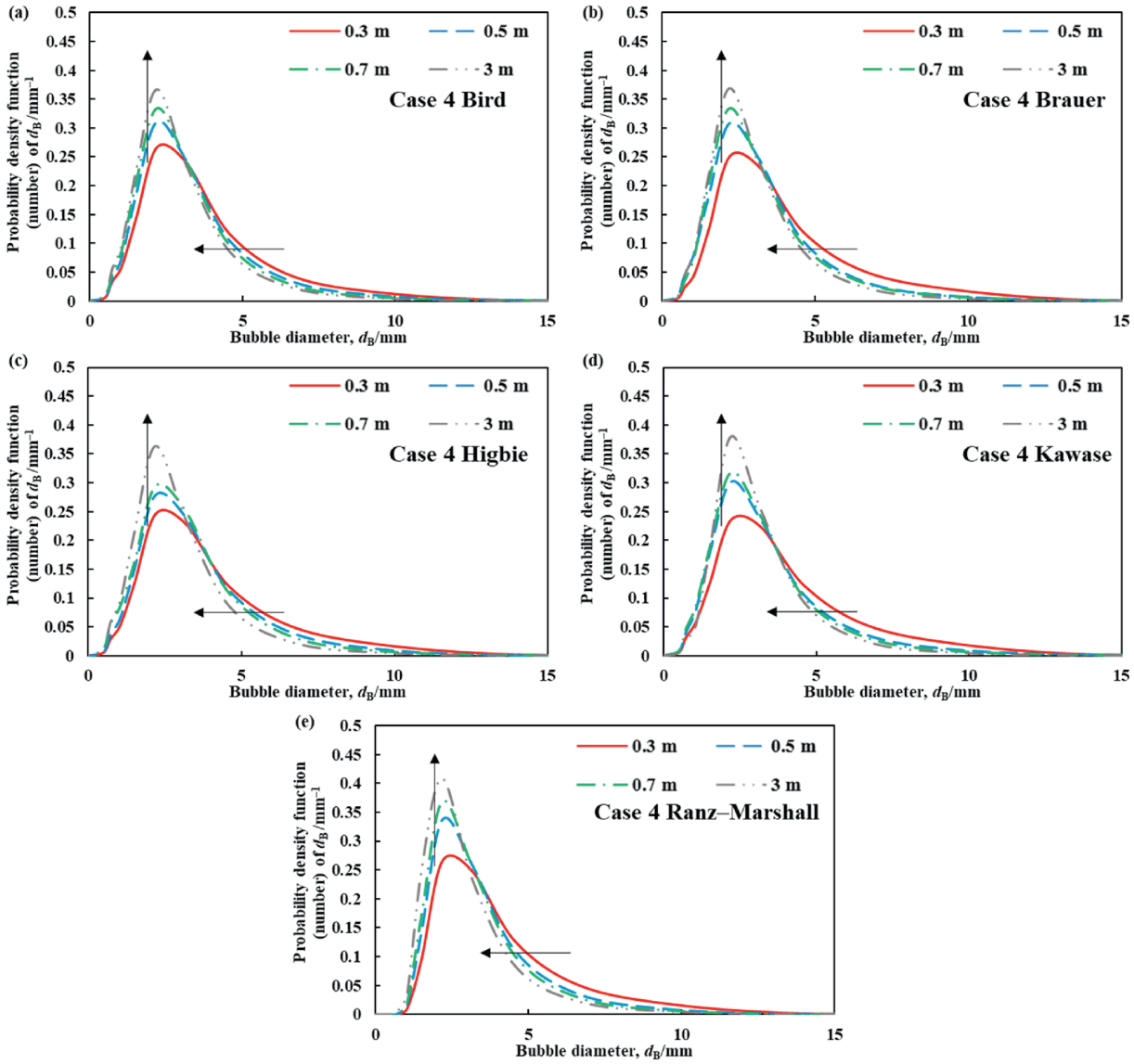

Fig. 18. Bubble size distributions at different heights with various mass transfer models: (a) Bird, (b) Brauer, (c) Higbie, (d) Kawase, and (e) Ranz–Marshall for case 4.

interactions and bubble behaviors at different heights within the bubble column under different cases.

3.6. Error analysis

Fig. 19 shows parity graphs of gas holdup and mass fraction of CO_2 in gas phase using different mass transfer models. Among 4 cases, the gas holdup of case 2 was not measured in the reference. The simulation results of Kawase model, including mass fraction of CO_2 in gas phase and gas holdup agree with experimental data within ±15% error range. The majority of simulated data from the Higbie model agree with experimental data within ±20% error range, while a small portion of the data falls within ±60% error range. The predictive precision of the Brauer model is very close to that of the Bird model, with error range from ±30% to ±60%. However, the Ranz–Marshall model's errors significantly exceed ±500%, rendering its results evidently unreliable. Therefore, the Kawase model is highly suggested for simulating the mass transfer in co-current or counter-current bubble columns. The mass transfer models that include the turbulence effects, such as eddy currents, are promising and worth of further development.

The eddy cell model (*i.e.*, the Kawase model) posits that small-scale eddies play a dominant role in mass transfer, with turbulent kinetic energy and dissipation rate serving as key influencing factors. In contrast, other models, including those by Higbie, Bird, Brauer, and Ranz–Marshall, yield comparatively poor predictions. These models are primarily based on single-bubble mass transfer theory and rely on parameters such as bubble diameter, shape, slip velocity, and *Re*. Consequently, they fail to adequately represent the behavior of bubble swarms or capture the influence of turbulence on interphase mass transfer.

3.7. Effects of operation modes on mass transfer

To discuss the effect of operation modes on mass transfer, the simulated results of a co-current and a counter-current gas absorption cases 1 and 5 using Kawase model are examined in depth.

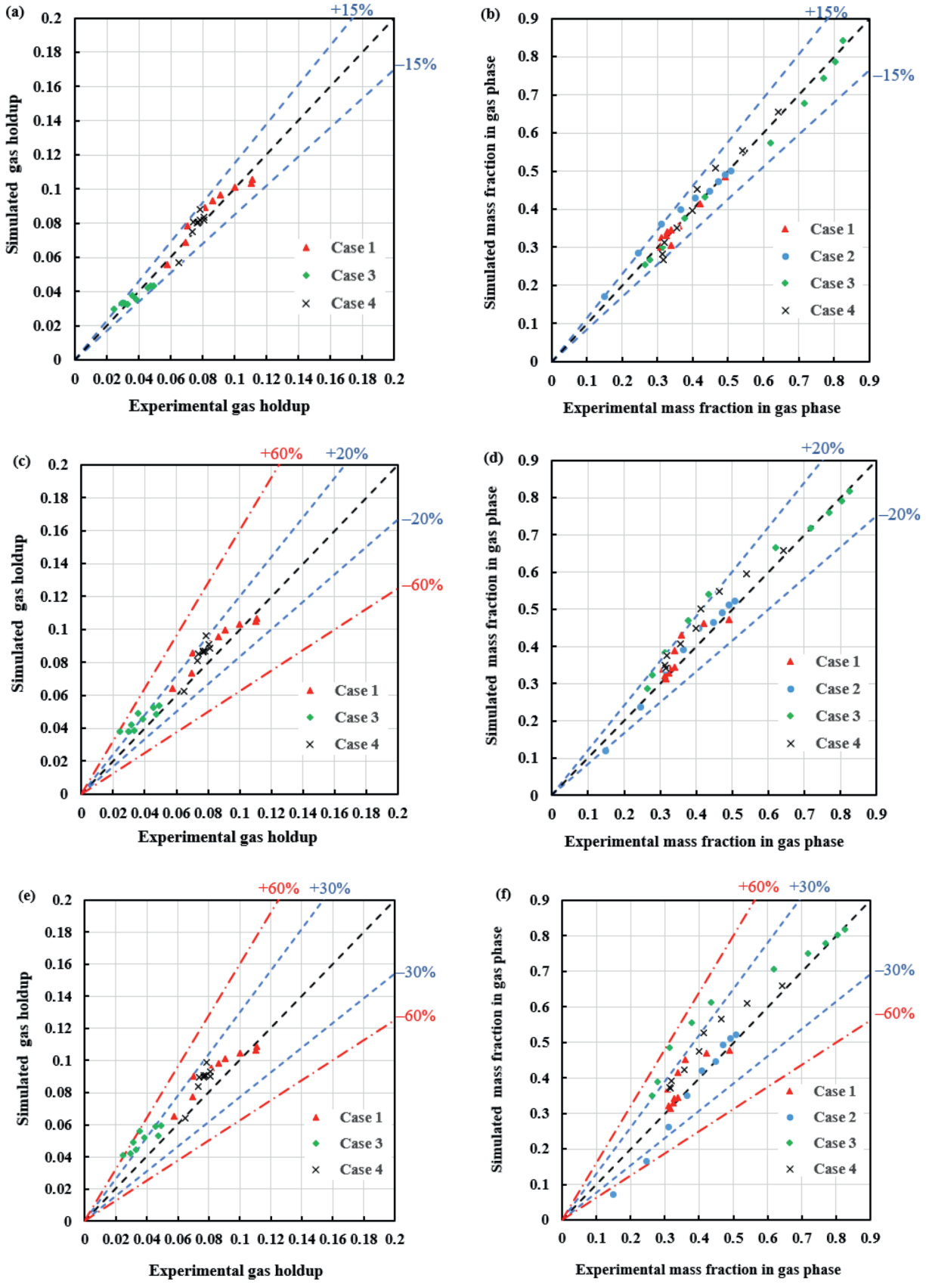

Fig. 19. Parity graphs of experimental data and computed results for 4 cases using different mass transfer models: (a)(b) Kawase, (c)(d) Higbie, (e)(f) Bird, (g)(h) Brauer, and (i)(j) Ranz–Marshall.

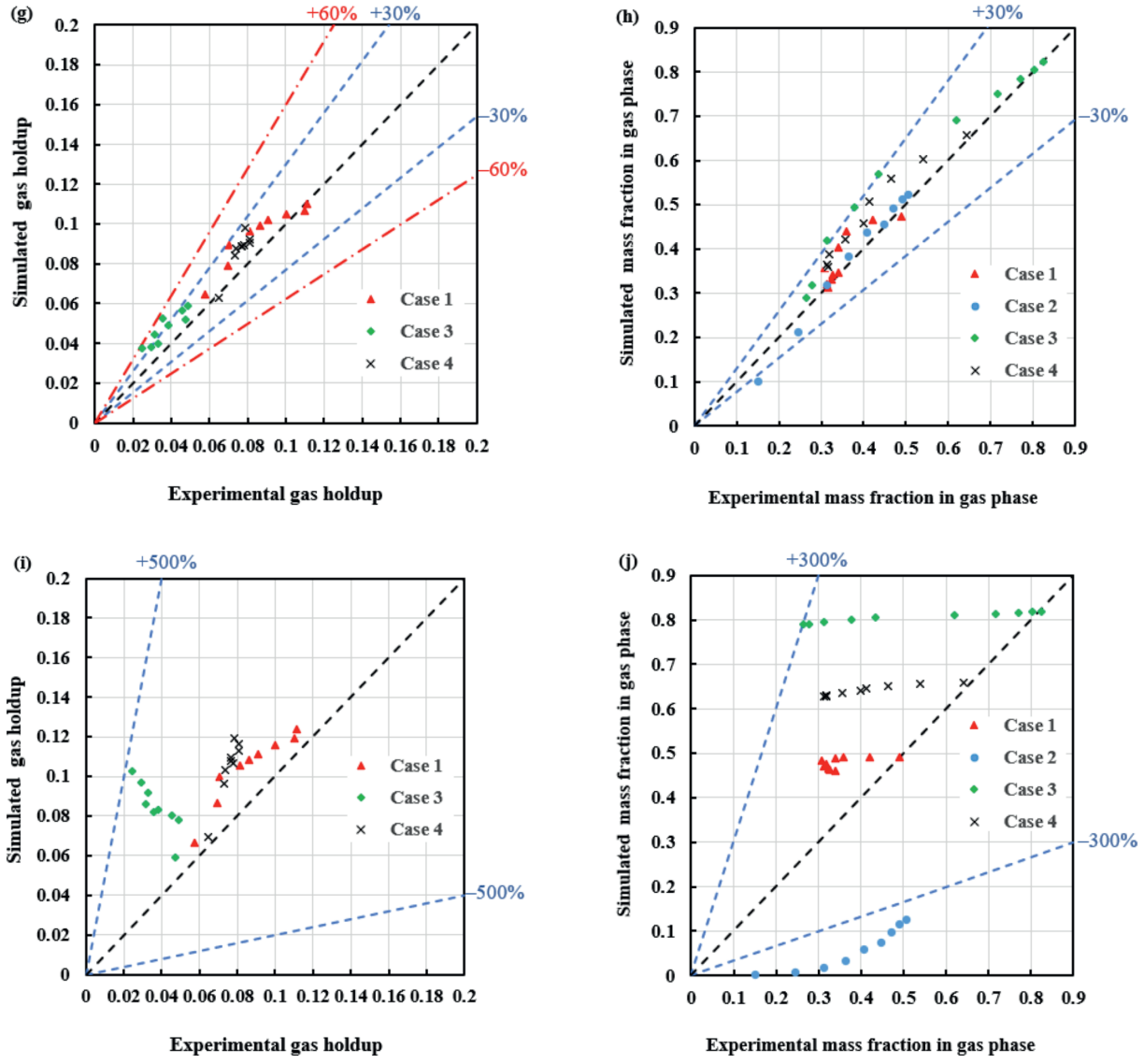

Fig. 19. (*continued*).

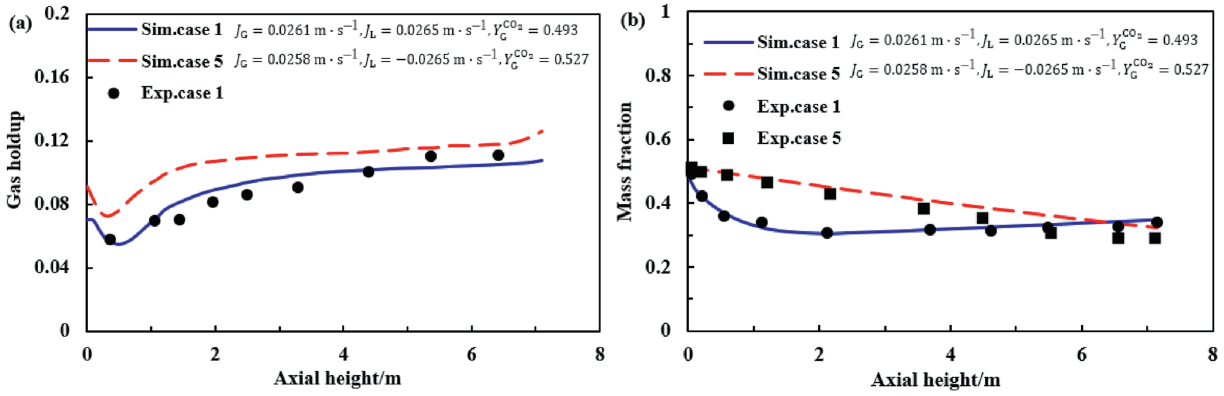

Fig. 20. Comparisons between simulated results and experimental data with the Kawase model in case 1 and case 5: (a) gas holdup, and (b) mass fraction of CO_2 in the gas phase.

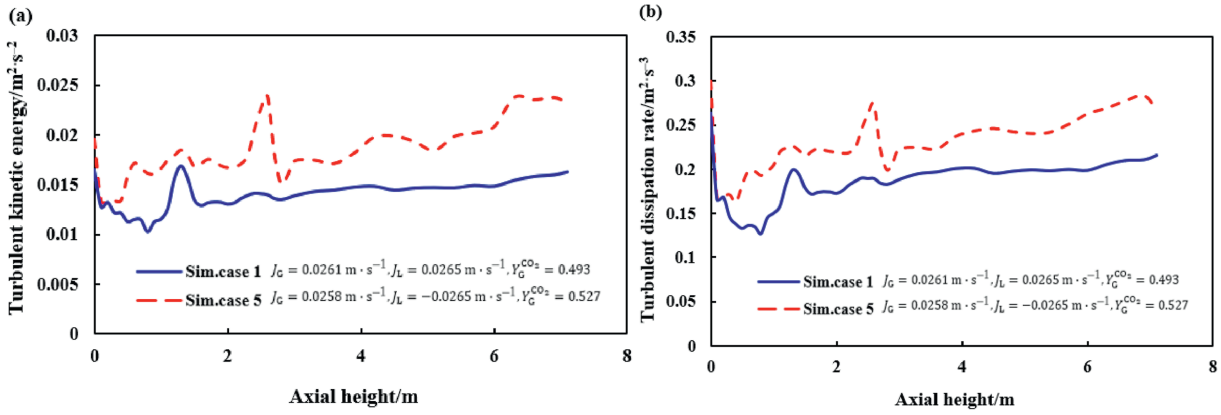

Fig. 21. Comparisons of simulated results with Kawase model in co-current mode and counter-current mode along the height of bubble column: (a) turbulent kinetic energy, and (b) turbulent dissipation rate.

The 2 cases were operated with similar conditions (gas velocity, liquid velocity and CO_2 mass fraction), but show significant differences in simulated gas holdup and mass transfer rates. Fig. 20(a) and (b) compare the calculated gas holdup and the mass fraction of CO_2 in gas phase for the two cases, respectively. From Fig. 20, the gas holdup of the counter-current flow is larger than that of co-current flow. Because the reverse flow of the two gas–liquid phases decelerate the bubbles and takes longer time to reach the bubble terminal velocity. In simulations, the volume-average result of mass fraction of CO_2 in liquid phase of cases 1 and 5 are 4.6×10^{-4} and 5.8×10^{-4} respectively. It clearly shows that the global mass transfer flux of the counter-current flow is higher than the co-current flow, and the counter-current flow promote mass transfer effectively, partly due to a higher gas holdup. The turbulence might also play a vital role in promoting interface mass transfer. Fig. 21(a) and (b) present the turbulence kinetic energy k and the dissipation rate ε along the height of bubble column. The turbulence in a counter-current operation is significantly stronger than that of a co-current mode, especially for the bottom half of the bubble column. It is observed the stronger the turbulence the higher the mass transfer rates. The results further confirm that Kawase model that has taken the turbulence into account performed reliably.

Results in this section offers direct design guidance: counter-current bubble columns are recommended to maximize mass transfer rates and gas holdup, making them particularly suitable for applications such as gas absorption, desulfurization, and biochemical water treatment. Conversely, co-current operation is advised for processes in which minimizing energy consumption is the primary objective, such as those in the chemical and metallurgical industries.

The findings presented in this section provide practical design guidance for bubble column operation. To maximize mass transfer rates and gas holdup, the counter-current mode is highly recommended. This configuration is particularly advantageous for applications such as gas absorption, desulfurization, and biochemical water treatment. On the other hand, co-current operation is preferable when minimizing energy consumption is the primary concern, as commonly required in certain chemical and metallurgical processes.

It is important to note that the initial bubble diameters were calculated by using the Polli correlation as 9.6, 5.6, 7.9, 8.8, and 9.6 mm for the respective cases. However, both the predicted and experimentally measured bubble diameters were approximately 3 mm. This obvious reduction suggests that intensive bubble breakup occurs within the column. Additional simulations were carried out and shown in Supplementary Material S2. Results show that bubble breakup model critically influences both bubble dynamics and gas–liquid mass transfer. This underscores the need of greater efforts to be directed toward understanding the mechanism of bubble breakup.

4. Conclusions

CFD-PBM is employed to analyze interphase mass transfer in co-current and counter-current bubble columns using three types of mass transfer models. The simulation results were compared with spatial distribution data and volume mass transfer coefficient from literature under different operating conditions. The effects of co-current and counter-current flow modes on mass transfer were explored. The validated model offers a foundation for future studies on reactive systems, high-viscosity liquids and non-Newtonian fluids.

The following conclusions were obtained:

(1) The Kawase model provided reasonable prediction of mass transfer in co- and counter-current bubble column, with deviations from experimental data typically within ±15%. The model outperformed over other models due to a proper description of effects of turbulence on mass transfer in bubble column flows.
(2) The Brauer model, the Bird model and the Higbie model can predict the general trend of mass transfer processes in both co-current and counter-current flow. However, due to their significant errors, these three models are not recommended to use for simulation purposes. Ranz–Marshall model incorrectly predicts the entire gas–liquid mass transfer.
(3) The bubble size distribution in co-current and counter-current bubble columns varies under different operating conditions, which may be attributed to various factors such as gas–liquid interactions, bubble coalescence and break-up behaviors, and gas–liquid mass transfer processes.
(4) Compared with co-current flow, counter-current flow can enhance the gas–liquid mass transfer process by increasing the gas holdup and intensifying turbulence.

CRediT Authorship Contribution Statement

Keran Li: Writing – original draft, Validation, Investigation, Conceptualization. Xi Ma: Validation, Investigation. Shuai Yan: Investigation. Caixia Chen: Writing – original draft, Supervision,

Methodology. Zihong Xia: Writing – review & editing, Writing – original draft, Supervision, Methodology.

Declaration of Competing Interest

The authors declare that they have no known competing financial interests or personal relationships that could have appeared to influence the work reported in this paper.

Nomenclature

a	interfacial area concentration, m^{-1}
$b(V')$	the breakup rates of bubbles, $m^3 \cdot s^{-1}$
C_D	the drag coefficient
C_{VM}	the virtual mass coefficient
$C_{1\varepsilon}$	the model constants of the dispersed RNG $k-\varepsilon$ model
$C_{2\varepsilon}$	the model constants of the dispersed RNG $k-\varepsilon$ model
C_μ	the model constants of the dispersed RNG $k-\varepsilon$ model
c	coalescence frequency, s^{-1}
$c(V,V')$	the coalescence rates of bubbles, $m^3 \cdot s^{-1}$
D	diffusion coefficient, $m^2 \cdot s^{-1}$
d	diameter of the mother bubble, m
d_B	bubble diameter, m
$d(b)$	overall breakup frequency of bubbles with diameter d, s^{-1}
f_v	fragmentation ratio
$G_{k,L}$	the generation of turbulence kinetic energy due to the mean velocity gradients
G_V	the particle volume-based growth rate, $m^3 \cdot s^{-1}$
$\boldsymbol{g}$	acceleration of gravity, $m \cdot s^{-2}$
He	Henry constant
K_{GL}	the covariance of the velocities of the continuous phase and the dispersed phase
k	turbulent kinetic energy, $m^2 \cdot s^{-2}$
k_L	liquid-side mass transfer coefficient, $m \cdot s^{-1}$
$\boldsymbol{M}$	inter-phase momentum exchange, $N \cdot m^{-3}$
$\dot{m}$	the mass source term, $kg \cdot m^{-3} \cdot s^{-1}$
$n(V,t)$	the number density of bubbles of volume V per unit flow field space
$P_{c,ij}$	the product of the coalescence efficiency
p	pressure, Pa
R	universal gas constant, $J \cdot mol^{-1} \cdot K^{-1}$
Re	Reynolds number
Sc	Schmidt number
T	temperature, K
t	time, s
U	superficial velocity, $m \cdot s^{-1}$
U_{slip}	slip velocity, $m \cdot s^{-1}$
$\boldsymbol{u}$	velocity vector, $m \cdot s^{-1}$
X	mole fraction
Y	mass fraction
α	volume fraction
$\beta(V,V')$	the daughter size distribution
ε	turbulent dissipation rate, $m^2 \cdot s^{-3}$
η	Kolmogorov length scale, m
μ	dynamic viscosity, Pa·s
$\mu_{m,L}$	molecular viscosity of liquid phase, Pa·s
$\mu_{t,L}$	turbulent viscosity of liquid phase, Pa·s
ξ	dimensionless eddy scale
ν	kinematic viscosity, $m^2 \cdot s^{-1}$
ρ	density, $kg \cdot m^{-3}$
σ	surface tension, $N \cdot m^{-1}$
σ_k	the turbulent Prandtl numbers for k
σ_ε	the turbulent Prandtl numbers for ε
$\omega_{c,ij}$	the collision frequency between bubbles, $m^{-1} \cdot s^{-1}$
$\Pi_{k,L}$	the source terms for bubble induced turbulence for k
$\Pi_{\varepsilon,L}$	the source terms for bubble induced turbulence for ε

Subscripts

G	gas phase
i	group i
j	group j
L	liquid phase
q	phase q

Superscripts

CO_2	carbon dioxide
s	species s

Supplementary Material

Supplementary data to this article can be found online at https://doi.org/10.1016/j.cjche.2025.09.021.

References

[1] F. Hernandez-Alvarado, D.V. Kalaga, S. Banerjee, M. Kawaji, Comparison of gas hold-up profiles in co-current, counter-current and batch bubble column reactors measured using gamma densitometry and the surface of revolution method, In: ASME 2016 Fluids Engineering Division Summer Meeting Collocated with the ASME 2016 Heat Transfer Summer Conference and the ASME 2016 14th International Conference on Nanochannels, Microchannels, and Minichannels, Washington, DC, USA (2016).
[2] G. Besagni, F. Inzoli, Comprehensive experimental investigation of counter-current bubble column hydrodynamics: holdup, flow regime transition, bubble size distributions, and local flow properties, *Chem. Eng. Sci.* 146 (2016) 259–290.
[3] P. Rollbusch, M. Becker, M. Ludwig, A. Bieberle, M. Grünewald, U. Hampel, R. Franke, Experimental investigation of the influence of column scale, gas density and liquid properties on gas holdup in bubble columns, *Int. J. Multiphas. Flow* 75 (2015) 88–106.
[4] G. Besagni, Bubble column fluid dynamics: a novel perspective for flow regimes and comprehensive experimental investigations, *Int. J. Multiphas. Flow* 135 (2021) 103510.
[5] T. Ziegenhein, D. Lucas, G. Besagni, F. Inzoli, Experimental study of the liquid velocity and turbulence in a large-scale air–water counter-current bubble column, *Exp. Therm. Fluid Sci.* 111 (2020) 109955.
[6] R.F. Mudde, T. Saito, Hydrodynamical similarities between bubble column and bubbly pipe flow, *J. Fluid Mech.* 437 (2001) 203–228.
[7] L.C. Han, J. Fu, M. Li, S.G. Gong, N.N. Gao, C. Zhang, H.A. Luo, A theoretical unsteady-state model for k_L of bubbles based on the framework of wide energy spectrum, *AIChE J.* 62 (4) (2016) 1007–1022.
[8] G.E. Fortescue, J.R.A. Pearson, On gas absorption into a turbulent liquid, *Chem. Eng. Sci.* 22 (9) (1967) 1163–1176.
[9] R. Rzehak, E. Krepper, Euler–Euler simulation of mass-transfer in bubbly flows, *Chem. Eng. Sci.* 155 (2016) 459–468.
[10] A.M. Hissanaga, N. Padoin, E.E. Paladino, Mass transfer modeling and simulation of a transient homogeneous bubbly flow in a bubble column, *Chem. Eng. Sci.* 218 (2020) 115531.
[11] Z.J. Chen, X.R. Zhang, B.S. Su, Influence of arc baffle configuration on gas–liquid mass transfer in flat-plate bubble column, *Chem. Eng. Res. Des.* 165 (2021) 129–136.
[12] H. Khan, R. Lehnigk, R. Rzehak, Euler–Euler simulation of absorption and desorption in co- and counter-current bubble column flows, *Chem. Eng. Sci.* 267 (2023) 118313.
[13] L. Zhao, Y. Lu, D.L. Lu, Z.Y. Tang, Modelling for gas–liquid bubbling flow and mass transfer with OpenFOAM, *Int. J. Multiphas. Flow* 163 (2023) 104441.
[14] W.E. Ranz, W.R. Marshall, Evaporation from drops: part I, *Chem. Eng. Prog.* 48 (3) (1952) 141–146.
[15] H. Brauer, Particle/fluid transport processes, *Chem. Eng. Prog.* 19 (1981) 61–99.
[16] R. Higbie, The rate of absorption of a pure gas into a still liquids during short periods of exposure, *Trans. Am. Inst. Chem. Eng.* 31 (1935) 365–389.
[17] R.B. Bird, Transport phenomena, *Appl. Mech. Rev.* 55 (1) (2002) R1–R2.
[18] P.V. Danckwerts, Significance of liquid-film coefficients in gas absorption, *Ind. Eng. Chem. Res.* 43 (6) (1951) 1460–1467.
[19] J.C. Lamont, D.S. Scott, An eddy cell model of mass transfer into the surface of a turbulent liquid, *AIChE J.* 16 (4) (1970) 513–519.
[20] Y. Kawase, B. Halard, M. Moo-Young, Theoretical prediction of volumetric mass transfer coefficients in bubble columns for Newtonian and non-Newtonian fluids, *Chem. Eng. Sci.* 42 (7) (1987) 1609–1617.

[21] R.S. Tang, C. Cui, D.X. Zhang, D.G. Li, J.Y. Li, X.Y. Xu, Experimental and CFD simulation study of the air-blowing process of iodine in nitric acid solution, *Ind. Eng. Chem. Res.* 61 (36) (2022) 13694−13709.
[22] Z. Hao, L.B. Yang, S.T. Xiao, X.C. Liu, W.L. Zhao, CFD-PBE simulation of flow dynamics and mass transfer in two-stage countercurrent mixer-settler, *Ind. Eng. Chem. Res.* 62 (26) (2023) 10237−10251.
[23] P. Ranganathan, Numerical simulation of a gas−liquid oscillatory baffled column focusing on hydrodynamics and mass transfer, *Ind. Eng. Chem. Res.* 61 (26) (2022) 9443−9455.
[24] S. Kouzbour, F. Maniscalco, A. Buffo, M. Vanni, F.X. Grau, B. Gourich, Y. Stiriba, Effects of SDS surface-active agents on hydrodynamics and oxygen mass transfer in a square bubble column reactor: experimental and CFD modeling study, *Int. J. Multiphas. Flow* 165 (2023) 104486.
[25] H.H. Zhang, K.Y. Guo, Y.L. Wang, A. Sayyar, T.F. Wang, Numerical simulations of the effect of liquid viscosity on gas−liquid mass transfer of a bubble column with a CFD-PBM coupled model, *Int. J. Heat Mass Tran.* 161 (2020) 120229.
[26] T.F. Wang, J.F. Wang, Numerical simulations of gas−liquid mass transfer in bubble columns with a CFD-PBM coupled model, *Chem. Eng. Sci.* 62 (24) (2007) 7107−7118.
[27] K.Y. Guo, T.F. Wang, Y.F. Liu, J.F. Wang, CFD-PBM simulations of a bubble column with different liquid properties, *Chem. Eng. J.* 329 (2017) 116−127.
[28] C.X. Li, Y.Z. Cui, X.G. Shi, J.S. Gao, X.Y. Lan, CFD simulation of mass transfer in bubble columns: detailed study of mass transfer models, *Chem. Eng. Sci.* 264 (2022) 118173.
[29] W.D. Deckwer, I. Adler, A. Zaidi, A comprehensive study on CO_2-interphase mass transfer in vertical cocurrent and countercurrent gas−liquid flow, *Can. J. Chem. Eng.* 56 (1) (1978) 43−55.
[30] A. Tomiyama, Struggle with computational bubble dynamics, *Multiphas. Sci. Technol.* 10 (4) (1998) 369−405.
[31] A. Tomiyama, H. Tamai, I. Zun, S. Hosokawa, Transverse migration of single bubbles in simple shear flows, *Chem. Eng. Sci.* 57 (11) (2002) 1849−1858.
[32] A.D. Burns, T. Frank, I. Hamill, J.M. Shi, The favre averaged drag model for turbulent dispersion in Eulerian multi-phase flows, In: 5th International Conference on Multiphase Flow, ICMF'04, Yokohama, Japan, 392 (2004).
[33] S. Hosokawa, A. Tomiyama, S. Misaki, T. Hamada, Lateral migration of single bubbles due to the presence of wall, In: ASME 2002 Joint U.S.-European Fluids Engineering Division Conference, Montreal, Quebec, Canada, (2002) https://doi.org/10.1115/FEDSM2002-31148.
[34] C. Laborde-Boutet, F. Larachi, N. Dromard, O. Delsart, D. Schweich, CFD simulation of bubble column flows: investigations on turbulence models in RANS approach, *Chem. Eng. Sci.* 64 (21) (2009) 4399−4413.
[35] L.J. Xu, Z.H. Xia, X.F. Guo, C.X. Chen, Application of population balance model in the simulation of slurry bubble column, *Ind. Eng. Chem. Res.* 53 (12) (2014) 4922−4930.
[36] A.A. Troshko, Y.A. Hassan, A two-equation turbulence model of turbulent bubbly flows, *Int. J. Multiphas. Flow* 22 (11) (2001) 1965−2000.
[37] N. Varallo, G. Besagni, R. Mereu, Computational fluid dynamics simulation of the heterogeneous regime in a large-scale bubble column, *Chem. Eng. Sci.* 280 (2023) 119090.
[38] Z.P. Yao, S. Yan, T. Wang, C.X. Chen, Z.H. Xia, Bubble breakup criteria for the population balance model of gas−liquid flow simulations, *Chem. Eng. Sci.* 280 (2023) 119078.
[39] G.F. Versteeg, W.P.M. van Swaaij, Solubility and diffusivity of acid gases (carbon dioxide, nitrous oxide) in aqueous alkanolamine solutions, *J. Chem. Eng. Data* 33 (1) (1988) 29−34.
[40] M. Polli, M. Di Stanislao, R. Bagatin, E. Abu Bakr, M. Masi, Bubble size distribution in the sparger region of bubble columns, *Chem. Eng. Sci.* 57 (1) (2002) 197−205.